doi:10.26443/seismica.v5i2.3190

Cell-Based Spectral Decomposition of Strong Ground Motion Data for Seismic Source and Attenuation Characterization in Italy

Dino Bindi * [1], **Giovanni Lanzano** [2], **Sara Sgobba** [2], **Francesca Pacor** [2]

[1]Helmholtz Centre for Geosciences GFZ, Potsdam, Germany, [2]Istituto Nazionale di Geofisica e Vulcanologia INGV, Milan, Italy

Author contributions: *Conceptualization*: Dino Bindi, Giovanni Lanzano, Sara Sgobba, Francesca Pacor. *Formal Analysis*: Dino Bindi. *Writing - Original draft*: Dino Bindi. *Writing - Review & Editing*: Dino Bindi, Giovanni Lanzano, Sara Sgobba, Francesca Pacor.

Abstract We apply the Generalised Inversion Technique (GIT) to decompose the Fourier amplitude spectra of the ITACAext dataset, comprising recordings of Italian earthquakes with magnitudes ≥ 3.0 since the 1970s. A cell-grid parameterization captures lateral attenuation variability, while a reference-event approach removes unresolved degrees of freedom. The resulting frequency-dependent attenuation coefficients reproduce the major tectonic attenuation domains of Italy. The estimated stress drop is largely magnitude independent, with an average value of $\Delta\sigma = 3.64$ MPa (10th-90th percentile range: 0.91–12.71 MPa). A modest increase is observed only for magnitudes above 4.6 (corresponding to a seismic moment of 10^{16} Nm), remaining within the overall variability. In contrast, stress drop shows pronounced spatial heterogeneity, reaching its highest average values in northern Italy and the Apulian foreland ($\Delta\sigma = 11.48$ and 9.33 MPa) and its lowest values in the eastern Ionian fault lobe and the Adriatic Sea zone ($\Delta\sigma = 1.50$ and 0.98 MPa). Comparison with a previously developed non-ergodic ground-motion model for Italy reveals strong consistency between the inferred attenuation and source parameters and the corresponding event- and path-specific residuals, both in their spatial distribution and in their event- and frequency-dependent correlations.

Production Editor: Andrea Llenos
Handling Editor: Pablo Heresi
Copy & Layout Editor: Aisling O'Kane

Received: July 10, 2026
Accepted: October 28, 2026
Published: November 20, 2026

1 Introduction

The development of ground-motion predictive models (GMPMs) has progressively shifted from traditional ergodic formulations toward non-ergodic approaches (e.g., Lavrentiadis et al., 2023), which explicitly account for systematic regional variations in seismic source, wave-propagation, and site effects. In this framework, recorded ground motions are commonly decomposed into source-, path-, and site-related components (Al Atik et al., 2010), allowing spatially coherent residuals to be modeled rather than treated as aleatory variability. While significant advances have been made in characterizing site-specific effects ($\delta S2S$), (e.g., Stewart et al., 2017; Sgobba et al., 2019; Chao et al., 2021; Sgobba et al., 2024), the physical interpretation and validation of path- and source-related terms in non-ergodic GMPMs remain challenging, particularly at the national scale.

Source effects play a fundamental role in controlling both the amplitude and spectral shape of ground motion, and their variability is commonly represented in GMPMs through between-event terms(δBe) and source-region adjustments (i.e., the location-to location term $\delta L2L$) Al Atik et al. (2010). However, these terms are often inferred statistically, with limited direct constraints from independently derived physical source parameters. The availability of a homogeneous catalog of seismic source properties, such as seismic moment, stress drop, and radiated energy, would provide an important benchmark for assessing the validity of source zonations adopted in non-ergodic GMPMs and for supporting the physical interpretation of model coefficients. Despite the existence of dense strong-motion networks in several regions, the availability of homogeneous catalogs compiled at the national scale remains limited, particularly in tectonically complex areas such as Italy, where studies often focus on specific tectonic domains or sequences.

Strong-motion spectral analysis provides a powerful tool to isolate source contributions from recorded ground motion, provided that path and site effects can be adequately separated. Among the available methodologies, the Generalized Inversion Technique (GIT) has been widely applied to decompose Fourier amplitude spectra (FAS) into source, attenuation, and site terms (e.g., Castro et al., 1990; Shearer et al., 2006; Edwards et al., 2008; Bindi and Kotha, 2020). GIT-based approaches have been used in a variety of tectonic settings and frequency ranges; however, they are inherently affected by trade-offs between model components and by the non-uniqueness of the solution (Bindi et al., 2024). In particular, assumptions regarding the spatial homogeneity of attenuation or the parameterization of path effects can strongly influence the resulting source spectra and, consequently, the inferred source parameters. To mitigate these limitations, several studies have introduced spatially variable attenuation models, including regionalized or cell-based parameterizations, which

*Corresponding author: dino.bindi@gfz.de

allow the propagation effects ($\delta P2P$) to vary laterally along the source-to-site paths (Dawood and Rodriguez-Marek, 2013; Grendas et al., 2022; Lavrentiadis et al., 2023; Chen et al., 2024; Bindi et al., 2025; Liu et al., 2025; Babič et al., 2026). In Italy, where strong lateral heterogeneities characterize both crustal structure and tectonic domains (Mele et al., 1997; Faccenna et al., 2014), such approaches are especially relevant. By discretizing the study area into a grid of cells and estimating attenuation parameters within each cell, it is possible to capture first-order spatial variability while maintaining a physically interpretable inversion framework.

To ensure a common data framework for comparing physical inversion parameters with GMPM residuals, in this study we analyze the national strong-motion dataset (ITACAext, Lanzano et al., 2025) to compile a comprehensive and homogeneous catalogue of seismic source parameters for seismic events of engineering interest in Italy since the 1970s. We apply a spatially-varying GIT framework combined with a cell-based description of seismic attenuation. Non-parametric source spectra are isolated from propagation and site effects by anchoring the source spectra of selected events to the results of a previous study (Bindi and Kotha, 2020) to resolve the inherent trade-off among the terms. For each event, seismic moment and corner frequency are estimated by fitting the non-parametric spectra to an ω^2 model (Brune, 1970, 1971). These parameters are subsequently used to compute additional source properties, including spectral stress drop, apparent stress, and Savage-Wood efficiency (Savage and Wood, 1971), the latter computed as the ratio of apparent stress to the stress drop. Finally, the resulting source parameters are spatially aggregated and mapped for different percentiles within the source-zonation polygons adopted for the development of non-ergodic GMPMs (Brunelli et al., 2023). This allows us to directly compare empirical source properties with spatial domain embedded in the non-ergodic formulation. The compiled catalog provides an independent, physically based constraint for evaluating source-region variability in Italy and offers new insights into the interpretation of source-related terms in non-ergodic ground-motion modeling. By linking empirical observations to regionalized physical processes, the results of this study serve a dual purpose. First, they provide a benchmark for interpreting and validating empirical GMPM. Second, they offer a rigorously constrained set of regionalized physical parameters that can be directly integrated into numerical simulations, bridging the gap between empirical seismological observations with predictive numerical simulations for seismic hazard applications

2 Data

In this study, we analyse ITACAext, a strong motion flatfile compiled for Italy (Lanzano et al., 2025). The following selections are applied: 1) Only events labeled as shallow crustal active are considered (2044 earthquakes); 2) Events from stations equipped with both a velocimeter and an accelerometer were not differentiated based on sensor type. ITACAext includes either the on-scale velocity recording, if available, or the acceleration recording, but never both for the same event; 3) The two horizontal components of the FAS are combined by computing the square root of the sum of their squares (i.e., vectorial sum).

Details of the data processing and flat file compilation can be found in Lanzano et al. (2025). Here, we outline only a few of the steps in their workflow that are important for the spectral analysis performed in this study. The FAS were computed for S-waves windows, and smoothed by applying the Konno and Ohmachi (1998) function with a smoothing parameter b set to 40. Signal trimming was performed using an energy-based criterion, whereby the cut times were identified from selected percentages of the total Arias Intensity (AI). The initial cut time (T_1) was defined at 1% AI for late-triggered records, 2.5% AI for stations with epicentral distance ($R_{epi} < 10$ km), and 5% AI for all other cases. The final cut time (T_2) was defined at 95% AI for $R_{epi} < 25$ km, 90% AI for $25 < R_{epi} < 50$ km, and 85% AI otherwise. To avoid excessively short records, when $dT = T_2 - T_1 < 5$ s, the final cut time was adjusted so that $dT = 5$ s. Since the traces were band-pass filtered, we analyze only the spectral amplitudes at frequencies within the passband of the filter, using the available information about the filter corner frequencies from the ITACAext flatfile. Furthermore, we only considered stations and events for which there were at least three recordings in the flatfile.

We analyzed a total of 1405 selected earthquakes (Figure 1a) in the moment magnitude range from 3 to 6.9 (with a median magnitude of 3.7 and 91 events with a magnitude of at least 5) recorded by 1585 stations (Figure 1b). There are 40102 spectral amplitudes available at 2 Hz. By considering a regular $0.2°x\ 0.2°$ grid and counting the number of rays crossing each cell, Figure 1c shows that the largest sampling is for Central Italy where the most recent sequences occurred (i.e., the 2009 L'Aquila and 2016-17 Amatrice-Visso-Norcia sequences). Finally, Figure 1d shows that the median of the epicentral distance distributions of the rays sampling each cell is highly spatially variable. This suggests that some areas are mostly sampled by long, deep rays (e.g., the Po Plain), while other regions are sampled by short rays traveling at shallower depths (e.g., central Italy).

3 Method

We assume that the spectral amplitude $FAS_{ij}(f)$ at a given frequency f for the event i as recorded by station j, can be expressed as the product of the source (S), propagation (P), and site (Z) terms (convolution theorem). Taking the logarithm of the product yields the following model for the spectral decomposition (GIT):

$$logFAS_{ij}(f) = logS_i(f) + logP_{ij}(f) + logZ_j(f) \quad (1)$$

By considering all the available combinations between i and j, equation 1 generates an overdetermined linear system that can be solved in a least squares sense (Stellato et al., 2020).

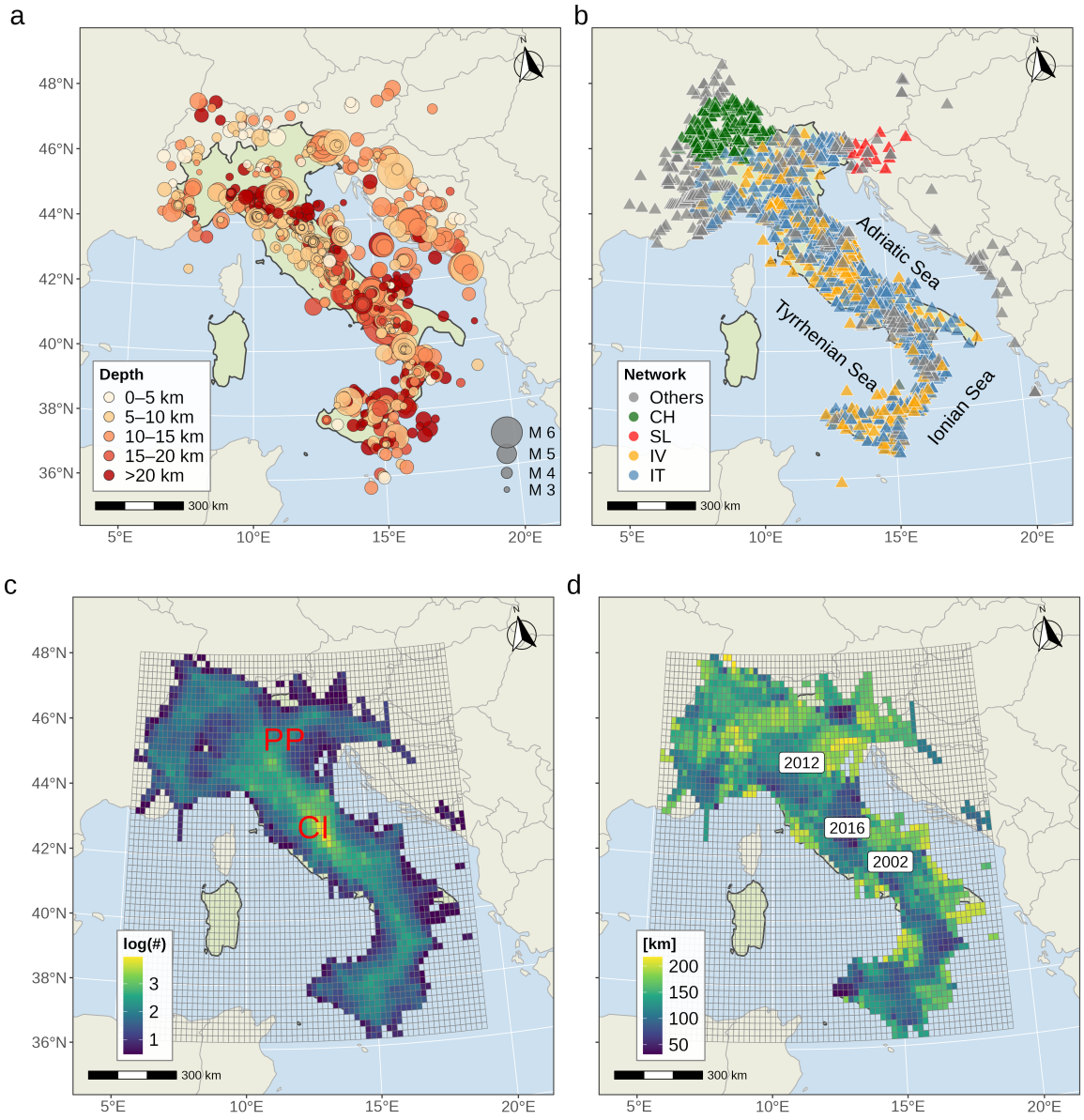


Figure 1 The data set and grid used for the analysis. Panel a shows the locations of the earthquakes used in this study, with the size of the symbols proportional to the magnitude and the colour representing the depth. Panel b shows the locations of the stations, with the colours indicating some of the main networks. Panel c illustrates the grid considered for the grid approach applied to compute the attenuation, with cell colour representing the number of rays crossing it. Labels indicate: PP- Po plain, CI- Central Italy. Panel d is the same as c, but colours represent the median length in km of the seismic rays crossing each cell. Labels 2012, 2016 and 2002 indicate the locations of the 2012 Emilia, 2016 Norcia and 2002 Molise earthquakes used as reference events for the spectral decomposition.

3.1 Cell-based attenuation

The path term $P_{ij}(f)$ in equation 1 is parametrized using the cell-based approach (Bindi et al., 2025):

$$logP_{ij}(f) = logG(R_{ij}; f) + \sum_{k}^{N_c} \lambda_{ijk}\alpha_k(f) \qquad (2)$$

where $G(R_{ij}; f)$ represents the geometrical spreading, α_k is the attenuation coefficient for cell k of the grid, and N_c is the total number of cells. According to equation 2, the attenuation term for the ij-th recording is computed as the integral over a straight line connecting the station j to the epicenter of event i, summing the attenuation values in the crossed cells and weighting them by λ. Two alternative choices are used for λ_{ijk}:

- in the mid-point approach, $\lambda_{ijk} = R_{ij}\delta_{k,MP}$ where R_{ij} is the hypocentral distance and δ is the Kronecker delta selecting the cell containing the mid-point (MP) of the segment connecting station j to event i (only one cell contributes to the sum in equation 2).
- in the intersection approach, $\lambda_{ijk} = \frac{R_{ij}}{R_{ij}^{epi}}\Delta_{ijk}$ where Δ_{ijk} is the length of the intersection between the horizontal line r_{ij} and cell k (all cells crossed by the ray contribute to the sum in equation (2) and $R_{ij}^{epi} = \sum_k \Delta_{ijk}$ is the epicentral distance.

The solution α is spatially smoothed by considering a Tikhonov penalization term. If we write equation 1 in matrix form as $\mathbf{A}\,\mathbf{m} = \mathbf{d}$, where $\mathbf{A}$ is the matrix of coefficients and $\mathbf{m}$ and $\mathbf{d}$ are the model and data vectors, respectively, then for the intersection approach, we consider the following problem:

$$\begin{bmatrix} \mathbf{A} \\ \gamma \mathbf{L} \end{bmatrix} \mathbf{m} = \begin{bmatrix} \mathbf{d} \\ \mathbf{0} \end{bmatrix} \tag{3}$$

where γ is a regularization parameter and the matrix L is the Laplacian operator applied to the attenuation coefficients α_k. After performing trial inversions with various values of γ and evaluating their performance in terms of residuals and the norm of the solution, we set γ to 100.

Regarding the geometrical spreading term G in equation 2, we consider a piece wise-linear model with two hinge distances (Bindi et al., 2017). After preliminary analysis and following indications from previous studies (Bindi et al., 2017), we set the hinges at $R_{h1} = 65$ km and $R_{h2} = 130$ km.

3.2 Non-uniqueness and constraints

Although the large number of recordings makes the linear system 1 overdetermined, a fully nonparametric approach introduces two unresolved degrees of freedom, causing the solution of system 1 to be nonunique (i.e., the matrix of coefficients A is not full rank). A typical constraint in nonparametric GIT is to require that the site amplification at one or more reference stations equals a fixed a priori spectral amplification function (e.g. Bindi et al., 2023). In this study, however, we apply a reference source constraint. To increase the number of stations affected by the constraints, we selected three reference earthquakes that occurred in the northern, central and southern Apennines (see Figure 1d for their locations). These events are the second mainshock of the 2002 Molise sequence; the first mainshock of the 2012 Emilia sequence; and the 2016 Norcia mainshock. We use the seismic moment and corner frequency from Bindi and Kotha (2020) to generate the reference source spectra assuming a Brune model (Brune, 1970). In particular, the moment magnitudes and corner frequencies used are:

- The Molise earthquake of 1 November 2002: Mw = 5.72, $f_c = 0.286$ Hz. It was a strike-slip event with strike 261°, dip 86° and rake −165° (Istituto Nazionale di Geofisica e Vulcanologia , 2025), with an hypocentral depth of 10 km.
- The 20 May 2012 Emilia earthquake: Mw = 6.09, $f_c = 0.220$ Hz. This was a thrust event with a strike of 103°, a dip of 25° and a rake of 87° (Cesca et al., 2013), with an hypocentral depth of 9.5 km.
- The 30 October 2016 Norcia earthquake: Mw = 6.5, $f_c = 0.154$ Hz. This is a normal fault earthquake with strike 148°, dip 41°, rake −104° (Pondrelli et al., 2012) and a depth of 6.2 km.

At each frequency, the source spectral values S_i for these three events are constrained to equal the reference values. Consequently, the source spectra produced in this study are consistent with those in Bindi and Kotha (2020).

3.3 Source parameters

The source spectra are fit in a least squares sense (Elzhov et al., 2023) to a ω^2 model to estimate the seismic moment M_o and the corner frequency f_c:

$$S(f) = \frac{\Omega^0}{[1 + (f/f_c)^2]} \tag{4}$$

$$\Omega^0 = \frac{R^{\theta\phi} F V}{4\pi\rho\beta^3} \frac{M_0}{r_{ref}} \tag{5}$$

$$r = \frac{k\beta}{f_c} \tag{6}$$

$$\Delta\sigma = \frac{7}{16} \frac{M_0}{r^3} \tag{7}$$

where we use an average radiation pattern $R^{\theta\phi} = 0.55$, a free surface amplification factor $F = 2$, an equipartition energy factor $V = 1$, an average density $\rho = 2600\ kg/m^3$, and an average shear wave velocity $\beta = 3400\ m/s$. The reference distance r_{ref} is set to 1km.

In equation 6, we use $k = 0.37$ (Brune, 1970, 1971) and the stress drop $\Delta\sigma$ in equation 7 is computed for a circular rupture with uniform stress drop (Eshelby, 1957). The radiated energy is computed from the integral of the squared velocity spectra (Izutani and Kanamori, 2001), applying a correction for the limited bandwidth effect (Ide and Beroza, 2001). Finally, apparent stress σ_a (Wyss, 1970) and the Savage-Wood efficiency η_{SW} (Savage and Wood, 1971) are computed as follows:

$$\sigma_a = \mu \frac{E_r}{M_0} \tag{8}$$

$$\eta_{sw} = \frac{\sigma_a}{\Delta\sigma} \tag{9}$$

where we set μ to 30 GPa.

4 Attenuation results

4.1 Mid-point versus intersection approach

Figure 2 compares the attenuation maps obtained for α at 10 Hz using the intersection and mid-point approaches. The maps show good overall agreement, displaying the same large-scale patterns. Figure 2c shows the normalized difference map, which reveals that the largest negative differences are localized at the boundaries of the regions sampled by the intersection approach but not well covered by the mid-point approach. The mean difference (bias) between the two maps is 4×10^{-4}, corresponding to a relative bias of -4.85% when computed with respect to the mean value of the

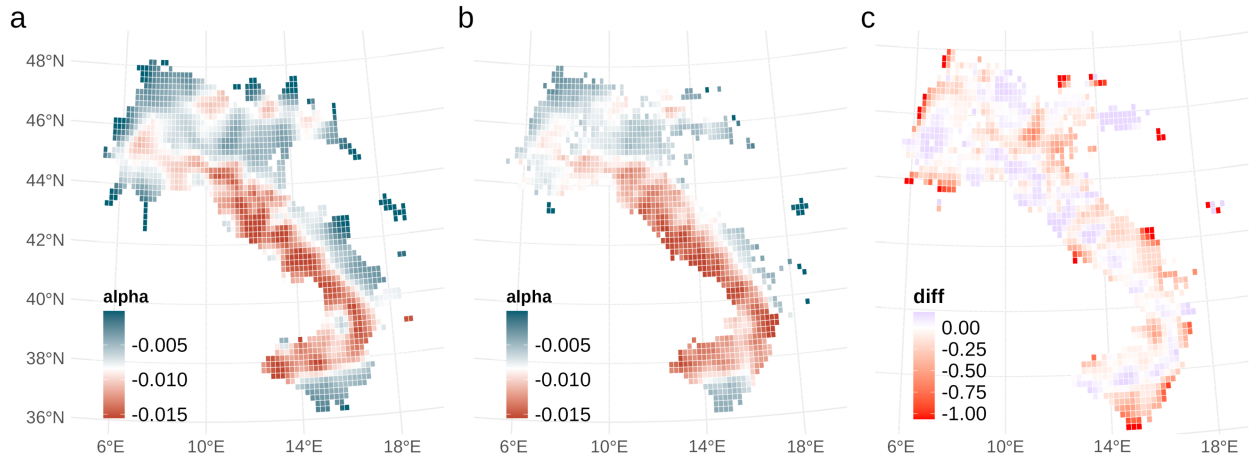


Figure 2 Comparison between the attenuation map at 10 Hz obtained with the intersection (panel a) and mid-point (panel b) approaches. Panel c shows the difference between the two approaches, normalised to the results for the intersection approach.

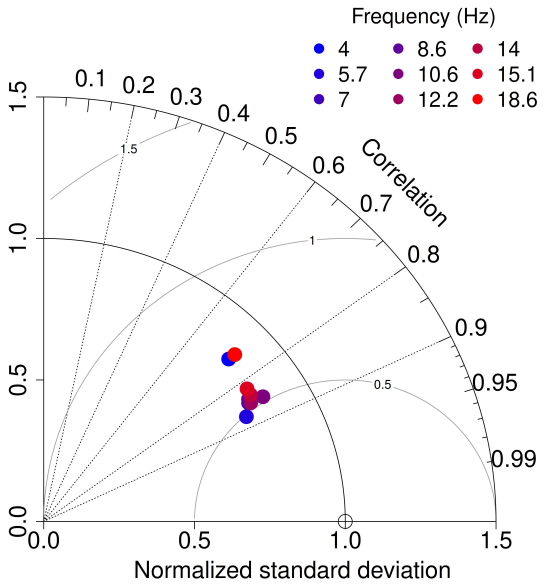


Figure 3 Taylor diagram (Taylor, 2001) computed by considering the intersection (reference model) and the mid-point maps for different frequencies (color points). The reference model corresponds to the point with coordinates $(x, y) = (1, 0)$. The Pearson correlation coefficient is related to the azimuthal angle. The normalized standard deviation of the mid-point solution is given by the radial distance from the origin. The normalized standard deviation of the intersection model is 1 by construction. The centered root-mean-squared error is proportional to the distance from the reference point on the x-axis.

intersection map. The mean absolute error (MAE) is 0.0012 and the root mean square error (RMSE) is 0.0016. The Pearson and Spearman correlation coefficients are 0.86 and 0.88, respectively, when the correlation between the two maps is computed. All these statistical measures of the similarity confirm that the two approaches provide highly consistent results. Comparisons for other frequencies show similar good agreement as shown by the Taylor diagram (Taylor, 2001) in Figure 3. The points indicating the results for the mid-point maps of frequencies between 5 and 15 Hz, where attenuation features are more evident and robust, cluster together. They have a similar Pearson correlation coefficient and a normalized standard deviation of approximately 80% of that of the intersection approach. Due to the similarity of the results, the remainder of this study will focus solely on the intersection approach.

4.2 Spatial distribution of attenuation coefficients

Figure 4 shows the maps for the attenuation coefficients α (equation 2) obtained with the intersection approach. Panels a to f show the results for frequencies ranging from 0.53 Hz to 19.90 Hz. The attenuation coefficients α are frequency dependent, increasing in absolute value with increasing frequency. Starting from around 2 Hz, spatial patterns clearly emerge, with stronger attenuation observed moving from the Apennines towards the Tyrrhenian Sea than the Adriatic Sea. Patterns are also evident in northern Italy between the Po Plain and the Alps to the north and the Apennines to the south. Furthermore, a strong attenuation contrast is observed in southern Italy when comparing northern Sicily to the southern sector of the island (i.e., the Hyblean Plateau). The geometrical spreading exponents exhibit stable behavior with respect to frequency. The slope n_1 for $R < 65km$ varies between 0.84 and 1.36. In particular, n_1 is almost constant and close to 1 for frequencies between 0.4 and 12 Hz, after which it steadily increases with frequency. For $65 < R < 130$ km, the slope n_2 is almost zero; and for $R > 130$ km, the slope n_3 varies between 0.2 and 0.3.

Figure 4 also shows the zones proposed by Brunelli et al. (2023) as a spatial grouping factor for describing the adjustments to the anelastic attenuation coefficient of a non-ergodic ground motion model derived for Italy. This zonation was constructed by simplifying the model proposed in Basili et al. (2019) and considering the spatial distribution of the correction δc_3 of the

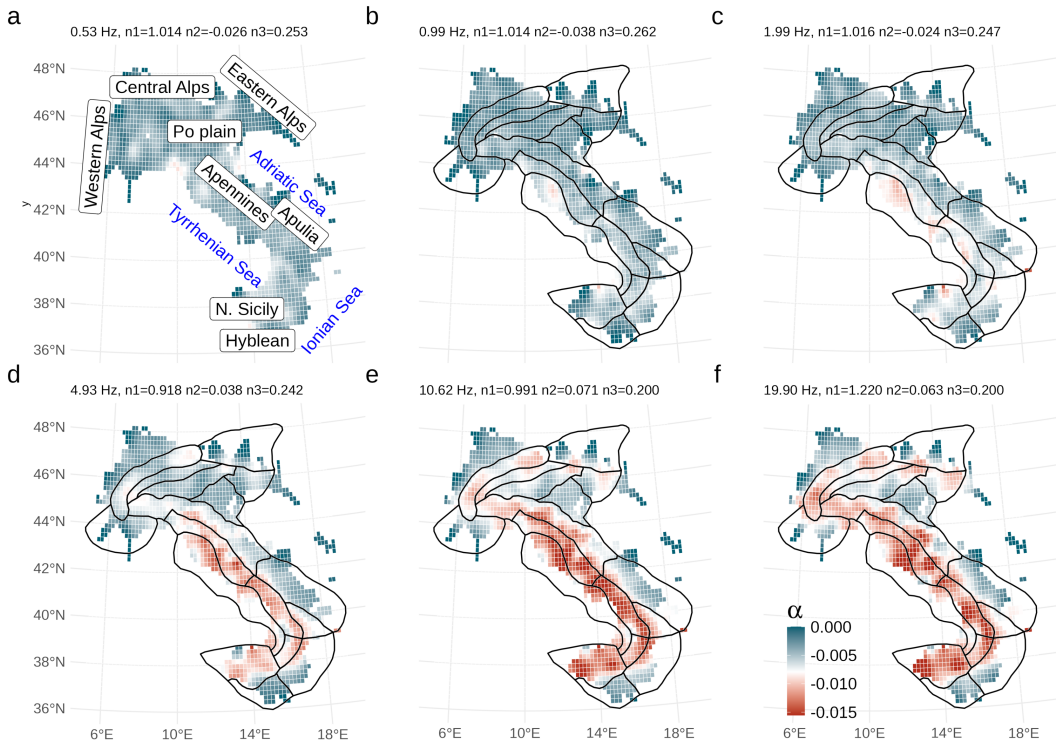


Figure 4 Attenuation maps at different frequencies, obtained using the intersection approach. The frequencies vary from 0.53 Hz (panel a) to 19.90 Hz (panel f), as indicated at the top of each panel, alongside the values of the geometrical spreading slopes, n_1, n_2 and n_3. The attenuation zonation used by Brunelli et al. (2023) is outlined in black. In panel a, the labels indicate some geographical locations mentioned in the text.

anelastic attenuation coefficient for source-station distances greater than 80 km (see equation 6 in Brunelli et al. (2023) for the definition of adjustments δc_3 for the anelastic coefficient c_3 of the GMPM).

There is good agreement between the zonation and the α spatial patterns at high frequencies, particularly in central and southern Italy. In northern Italy, some zones could be merged and others reshaped when analyzed in terms of α spatial variability. Figure 5 shows the inter-quartile ranges and median of α within each zone to quantify the variability of α within the zones. The map of the median confirms a stronger attenuation along the Tyrrhenian coast than the Adriatic coast, and a stronger attenuation in the northern than southern regions of Sicily. The spatial variability of the δc_3 values of Brunelli et al. (2023) (the numbers in Figure 5b) correlates well with the distribution of the median α. The most evident discrepancies occur in the Calabria and the Calabrian inner wedge zones. The former exhibits significant variability in the results according to Brunelli et al. (2023) (see their Figure 12) whereas the latter is not adequately covered in this study (see Figure 4). Figure 5d shows that the normalized inter-quartile range is relatively uniform across the zones, with the Adriatic south, the Calabrian inner wedge and the Hyblean plateau zones being the most variable.

Given the good sampling of the grid (see Figure 1c), we also performed an automatic zonation procedure (AZP) using a greedy algorithm (Openshaw, 1977) as implemented by Li and Anselin (2026). This heuristic approach searches for the optimal combination of spatial units in np regions (where np is fixed a-priori) by min-

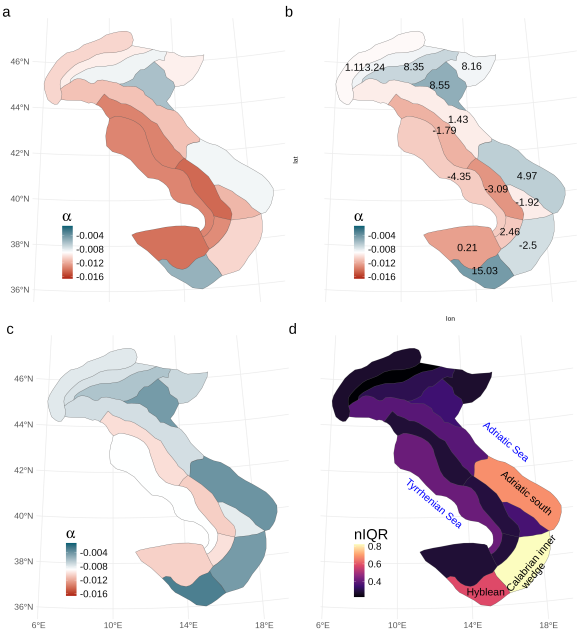


Figure 5 Percentiles of the attenuation coefficient α over each zone considered by Brunelli et al. (2023), considering the results for 19.90 Hz. Only zones covered by at least 50% of sampled grid cells are considered. Panels a to c show the $25th$ ($p25$), $50th$ ($p50$) and $75th$ ($p75$) percentiles, respectively. Panel d shows the normalized inter-quartile range, computed as $|p75 - p25|/p50$. The numbers in panel b represent the attenuation corrections $10^4 \delta c_3$ at high frequencies, taken from Table 2 in Brunelli et al. (2023). The zone names in panel d are also taken from the same reference.

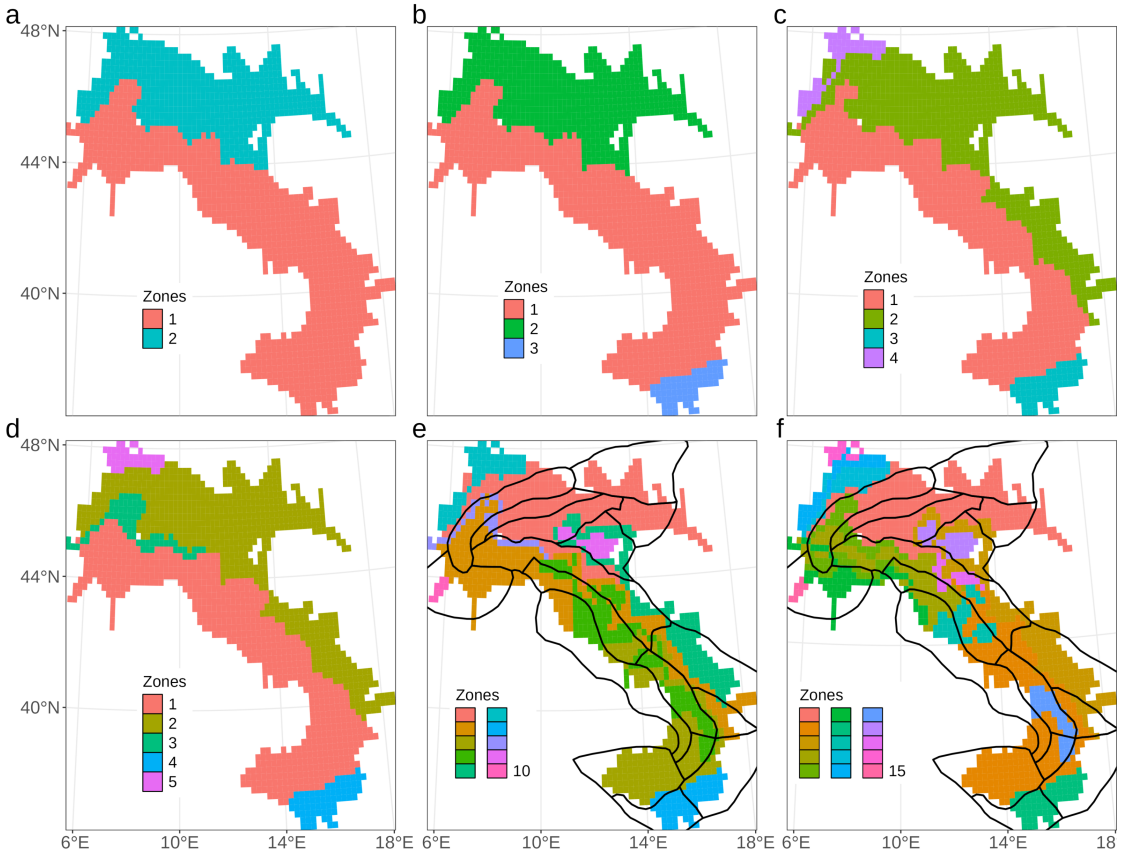


Figure 6 Results of the automatic zonation procedure applied to the attenuation coefficients α at 19.90 Hz. The number of zones considered varies from 2 (panel a) to 15 (panel f), as indicated by the legend in each plot. Panels e and f also show the (Brunelli et al., 2023) attenuation zonation in black.

imizing the within-unit sum of squares. We performed the AZP iteratively by increasing the number of regions, np. Figure 6 shows the results for np = 2,3,4,5,10 and 15, considering the results of 19.90 Hz. For np = 2, the two zones identified split the domain into a northern region including the Po plain and the central-eastern Alps, and the rest of Italy. Increasing np to 3 isolates the southern part of Sicily (Hyblean plateau). From np = 4, a longitudinal split is introduced along the Apennines into Tyrrhenian and Adriatic sides. For np = 5, a small domain in north-western Italy is introduced. Figure 6 also shows two attempts with large np values. These are not intended to identify a more resolved zonation that could lead to the over interpretation of the α maps, but rather to check whether the AZP refines in agreement with the Brunelli et al. (2023) zonation. Visual comparisons in Figures 6e and f show that the largest regions identified in the more refined α-driven zonation indeed agree well with the segmentation proposed by Brunelli et al. (2023).

5 Site amplifications results

Figure 7a shows that the site amplifications exhibit variability of more than a factor of 10 across the entire analysed frequency range, with different amplification patterns depending on local geological conditions. For example, the amplifications at station IT.NCR2.00.HN (Nocera Umbra) show a peak amplification of approximately 10 at 7 Hz. The shear wave velocity averaged over the uppermost 30 m (vs30) is 555 m/s and the strong amplification at high frequencies is consistent with class E of Eurocode 8 (ENV 1998-1-1, 1998), which is attributed to NCR2. Station IT.CLF.00.HN (Colfiorito; vs30 = 145 m/s; site class D of Eurocode 8) is characterised by a peak of amplification at 1 Hz, which is generated by edge-diffracted Love waves (Di Giulio et al., 2003). Station IT.NOR.00.HN (Norcia Castellina; vs30 = 423 m/s; site class B) is located in the Norcia basin, showing amplifications across a broad frequency range, from low to intermediate frequencies. This is due to deep sediments and 2D/3D effects (Bindi et al., 2011; Luzi et al., 2019). Figure 7a also shows the amplification at the rock stations CH.LLS.HG and IT.LSS.00.HN, which were used as reference stations in recent studies (Morasca et al., 2022; Yen et al., 2024). Consistently, these stations have some of the lowest amplifications, with almost a flat pattern. The estimated slopes of the high-frequency fall-off (Anderson and Hough, 1984) from the CH.LLS.HG and IT.LSS.00.HN amplification functions are $k_0 = 0.011 \pm 0.002$ s and $k_0 = 0.020 \pm 0.004$ s, respectively. This is consistent with the values used as constraints for the reference site amplifications in previous decompositions, e.g., $k_0 = 0.018$ s (Morasca et al., 2022). These results, along with the good agreement achieved for several other stations characterised in previous studies, support the reliability of the source-site decomposition.

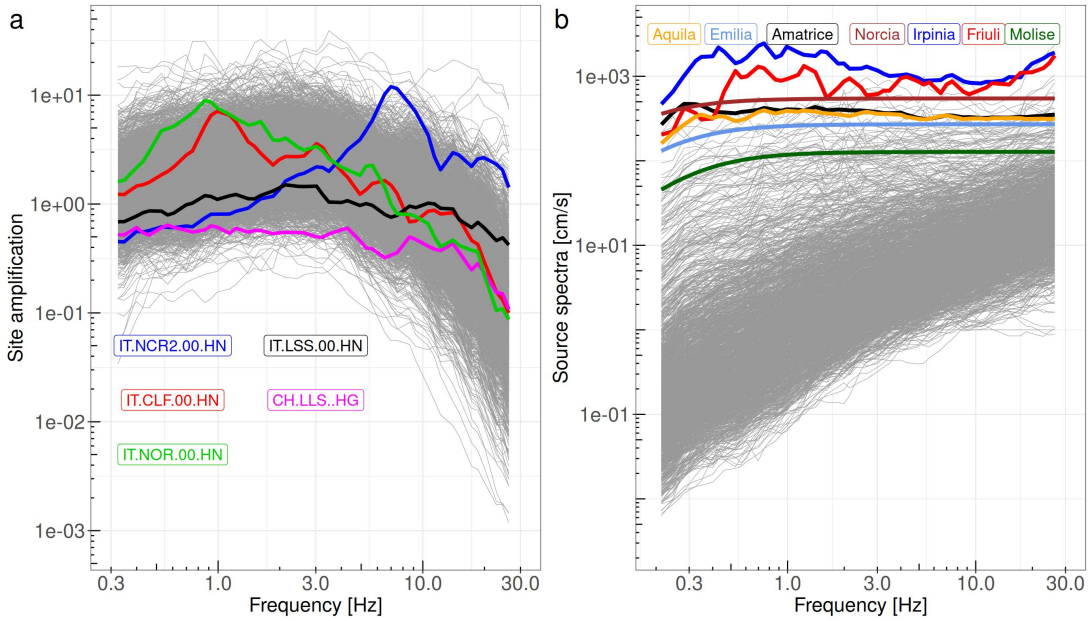


Figure 7 Site amplifications (panel a) and non-parametric source spectra (panel b) obtained by constraining the source spectra of the 2016 Norcia (brown), 2012 Emilia (light blue) and 2002 Molise (green) earthquakes to the results of Bindi and Kotha (2020) (see Figure 1d for their locations). The source spectra of the M_w 6.4, 1976 Friuli (red), the M_w 6.9, 1980 Irpinia (blue) and M_w 6.0, 2009 L'Aquila (orange) earthquakes are also highlighted.

6 Source results

Figure 7b shows the non-parametric source spectra obtained by constraining the spectral shape of three reference events to the results of Bindi and Kotha (2020). The spectra are fit to the ω^2 model (equation 4) to determine the seismic moment M_0 and the corner frequency f_c for each event. Then, the spectral stress drop $\Delta\sigma$ is computed using equation 7.

Figure 8 shows the scaling between the source parameters of 1346 earthquakes, selected requiring that the estimated corner frequency was greater than 0.05 Hz and the difference with the catalog magnitude was less than 0.6 in absolute value. Since limitations in the spectral bandwidth used for the fit could bias the estimation of f_c for small events (Kwiatek and Ben-Zion, 2016; Chen and Abercrombie, 2020; Bindi et al., 2020), the results for events with $f_c \geq 10$Hz are shown in orange in Figure 8 and not used for the statistical analysis. Figure 8 shows that:

- On average, $\Delta\sigma$ (panels a and b) is almost constant (self-similarity), with a slight tendency to increase for $M_0 \geq 10^{16}$ Nm (i.e., for $M_w \geq 4.6$). The 10th, 50th and 90th percentiles of the $\Delta\sigma$ distribution are 0.9080, 3.6406, and 12.7069 MPa, respectively. For $M_0 < 10^{16}$ Nm (1254 events), these percentiles are 0.8968, 3.6688 and 13.0002. Above 10^{16} Nm (92 events), they become 1.3269, 3.3230 and 8.5668. The results of a quantile regression performed considering the 2.5th, 50th and 97.5th percentiles (see red lines in Figure 8b) confirm that, while the median and the 97.5th percentile do not show significant changes, the 2.5th percentile remains almost constant for $M_0 < 10^{16}$ Nm and then it increases for larger events.
- The apparent stress σ_a (panel c) also shows a tendency to increase with seismic moment above 10^{16} Nm, and to remain almost constant between 10^{14} and 10^{16} Nm, where the median value is 0.7577 MPa. In terms of the scaled energy parameter, the median of the slowness parameter $\theta_k = log10(E_g/M_0)$ (Newman and Okal, 1998) approaches the value of -4.3 used by Kanamori (1977) to define the moment magnitude scale, when θ_k is averaged over the largest considered events (see magenta segments in Figure 8c). For example, the average θ_k computed considering events with $M_0 \geq 10^{17.5}$ Nm is $\theta_k = -4.39$. For $M_0 < 10^{16}$ Nm, the median value of θ_k is -4.55.
- In terms of efficiency (panel d), most of the values are below 0.3, with only a few events having an η_{SW} greater than 0.5 (i.e., under-shooting). Values for $M_0 > 10^{16}$ Nm are more scattered than those for smaller events, which show a more compact distribution with a median value of 0.24. It is worth noting that events with $\Delta\sigma \leq 2$ MPa are scattered above 10^{16} Nm (see red circles in Figure 8d), i.e., events with $\eta_{SW} < 0.2$ show a large variability in $\Delta\sigma$. The overall η_{SW} trend is similar to the σ_a trend.

Figure 9 shows the spatial distribution of $\Delta\sigma$. In order to remove the weak correlation between $\Delta\sigma$ and seismic moment, the right-hand panel shows the $\Delta\sigma$ residuals of the fitted linear model between $log\Delta\sigma$ and $logM_0$. Therefore, the map shows the deviations ϵ of $\Delta\sigma$ with respect to the expected values given the event magnitude. Some spatial patterns are evident in the map, with events in certain regions exhibiting consistently positive or negative residuals. To characterize the spatial clustering of the stress drop residuals, Figure 10 shows

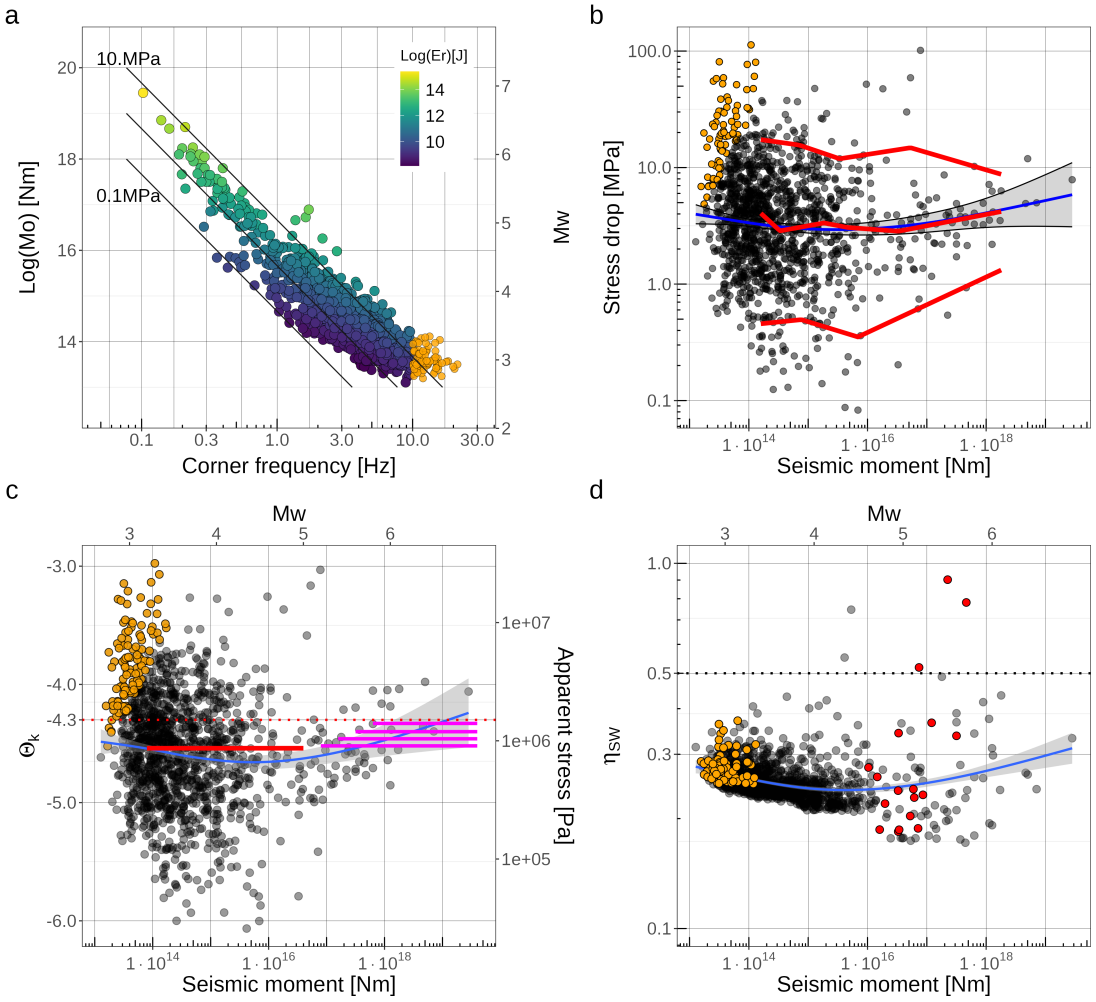


Figure 8 Panel a shows the seismic moment versus corner frequency scaling for 1346 earthquakes. The colors are proportional to the logarithm of the radiated energy. The straight lines show the scaling for a constant stress drop of 0.1, 1, and 10 MPa (equations 6 and 7). Panel b illustrates the stress drop versus seismic moment. Red lines represent the results of a quantile regression performed for the 2.5th, 50th, and 97.5th percentiles. Panel c shows the logarithm of the energy-to-moment ratio θ_k (left vertical axis) and apparent stress (right vertical axis) versus seismic moment. The red and magenta segments indicate the median θ_k over the corresponding seismic moment interval. Panel d shows the Savage-Wood efficiency (equation 9) versus seismic moment. The red circles indicate events with $\Delta\sigma \leq 2$ MPa. In all panels: orange symbols correspond to events with a corner frequency greater than 10 Hz, and the blue lines indicate the trend as determined by a Loess regression.

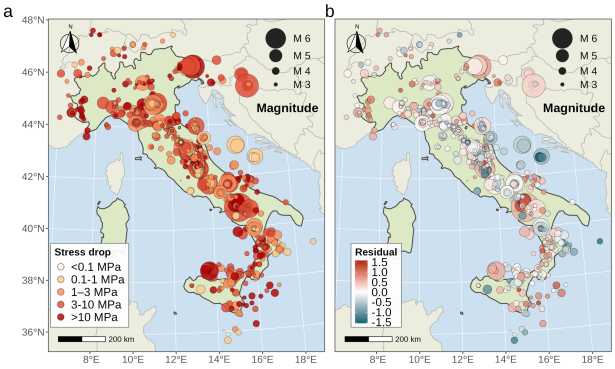


Figure 9 Panel a shows the stress drop $\Delta\sigma$ obtained for the 1346 earthquakes. Panel b illustrates the residuals of the stress drop calculated by fitting a linear model to remove the dependency of $log\Delta\sigma$ on $logMo$. The size of the symbols is proportional to the event magnitude.

the median and the interquartile range of the residuals grouped according to the source zonation proposed by Brunelli et al. (2023). This zonation was constructed by simplifying the seismogenetic zonation ZS16 proposed by Visini et al. (2022) for the MPS19 probabilistic hazard assessment of Italy and used by Brunelli et al. (2023) to provide a zonation for the between event residuals. They assigned to 17 zones the median between-event residual δB_e and the standard deviation of event and station corrected residuals δW_{es} (Al Atik et al., 2010), considering their non-ergodic GMPM for Italy.

Figure 10 shows that the zones in northern Italy (WA, GL, NA, and EA) have positive median and inter-quartile values. For example, the median ϵ for NA is 0.61, with inter-quartile range from 0.38 to 0.97. This corresponds to stress drops that are larger than the values expected for the corresponding magnitudes. In central Italy, the Adriatic Sea zone (AD) is characterized by negative residuals (stress drops that are lower than those predicted by the seismic moment dependent model), with

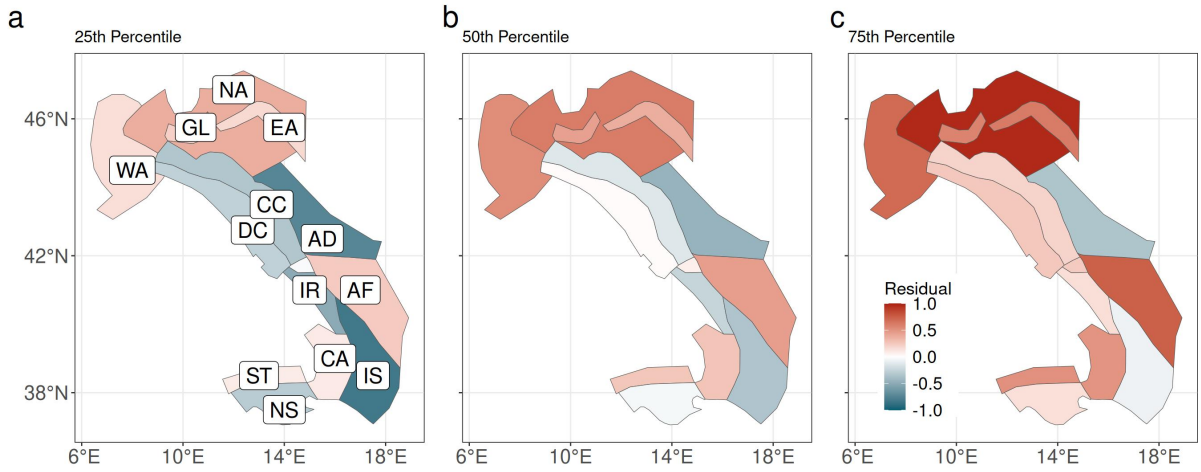


Figure 10 Percentiles of the stress drop residuals computed over the source zones proposed by Brunelli et al. (2023), with respect to the best-fit moment-magnitude-dependent model. Panel a shows the 25th percentile; panel b, the 50th percentile; and panel c, the 75th percentile. Only zones with at least 10 earthquakes are considered. Labels in panel a are taken from Brunelli et al. (2023): WA-Western Alps; NA- northern Italy; GL- Garda Lake; EA- Eastern Alps; DC- Distensive central-northern Apennines; CC- Compressive northern-central Apennines; AD- Central Adriatic Sea; IR- Irpinia and southern Apennines; AF- Apulian foreland; CA- Calabrian Apennine and southern Tyrrhenian Sea; IS- Ionian fault eastern lobe; ST- Southern Tyrrhenian; NS- Northern Sicily. See Table 1 in Brunelli et al. (2023) for a description of the zones and their connection with the ZS16 zonation used for seismic hazard assessment MS19 in Italy.

median $\epsilon = -0.45$ and inter-quartile range from -0.73 to -0.34, whereas the zones of the central Apennines fluctuate around zero. The large number of events located in these areas make them the reference areas for the average stress drop versus seismic moment model. In southern Italy, the Apulian foreland (AF), the Calabrian Apennine (CA) and the southern Tyrrhenian Sea (ST) zones exhibit positive residuals. For example, the median ϵ for AF is 0.46, with inter-quartile range from 0.24 to 0.74. In contrast, the median (ϵ=-0.34) and inter-quartile residuals for the Ionian Sea (IS) zone are negative (from -0.82 to -0.07). Overall, the spatial patterns of the stress drop residuals are in good agreement with the δB_e results of Brunelli et al. (2023) (their figures 5 and 8). In terms of absolute stress drops, the median values for NA and AF are $\Delta\sigma = 11.48$ and 9.33 MPa, respectivel, and are $\Delta\sigma = 0.98$ and 1.50 MPa, respectively, for AD and IS. In central Italy, $\Delta\sigma = 3.46$ and 2.39 MPa for zones DS and CC, respectively.

Finally, Figure 11 compares the source parameters with the between-event residuals δB_e computed by Brunelli et al. (2023), considering different frequencies. At 20 Hz, δB_e shows a positive correlation with $\Delta\sigma$ (panel a). This correlation weakens as the frequency decreases and becomes negligible at 2 Hz. For frequencies below 2 Hz, the correlation tends to become negative for small $\Delta\sigma$ values. When observed against seismic moment (panel b), the correlation is negligible at 20 Hz. For lower frequencies, a positive correlation emerges for events with M_0 lower than 10^{14} Nm. Panels c and d show the values of δB_e at 20 and 0.5 Hz against the difference between the catalog magnitude M_{cata} (i.e., the magnitude used to calibrate the GMPM) and Mw computed using the seismic moment estimated in this study. At 0.5 Hz, there is a negative correlation, which disappears at higher frequencies.

The correlation between δB_e and $\Delta\sigma$ at high frequencies has been discussed in several studies (e.g. Bindi et al., 2007; Baltay et al., 2013; Oth et al., 2017; Trugman and Shearer, 2018; Nie and Wang, 2025). Since the GMPM source scaling is controlled by the seismic moment, variations in the source radiation at high frequencies for events with the same moment magnitude are absorbed by δB_e. Conversely, any correlation between δB_e and $\Delta\sigma$ at low frequencies is not expected. To illustrate the sensitivity of the ω^2 source spectrum $S(f)$ on variation of $\Delta\sigma$ and M_0, panel e shows the partial derivatives of $logS(f)$ with respect to $log\Delta\sigma$ and $logM_0$ as a function of frequency. As the frequency f approaches 0, the sensitivity to $logM_0$ approaches 1, while the sensitivity to $log\Delta\sigma$ approaches 0. Thus, the low-frequency source spectrum is solely controlled by the seismic moment. Increasing the frequency, the sensitivity on $logM_0$ decreases while the sensitivity to $log\Delta\sigma$ increases. At $f = f_c$, the partial derivative of the log-spectrum with respect to log-seismic moment is 2/3 and the partial derivative of the log-spectrum with respect to log-stress drop is 1/3. At $f = \sqrt{3}f_c$, these partial derivatives are both 0.5. At high frequencies, both sensitivities converge to a constant value of 1/3 for $logM_0$ and 2/3 for $log\Delta\sigma$. Therefore, at high frequencies, the logarithm of the source spectrum depends on both $logM_0$ and $log\Delta\sigma$ with weights of 1/3 and 2/3, respectively. Since the median f_c of ITACAext data set is approximately 4 Hz, the decreases in the correlation between δB_e and $\Delta\sigma$ for frequencies decreasing from 20 to 2 Hz is consistent with the theoretical expectations in panel e.

However, the negative correlation at lower frequencies for small $\Delta\sigma$ values cannot be attributed to the direct impact of $\Delta\sigma$ variability on source spectra since the

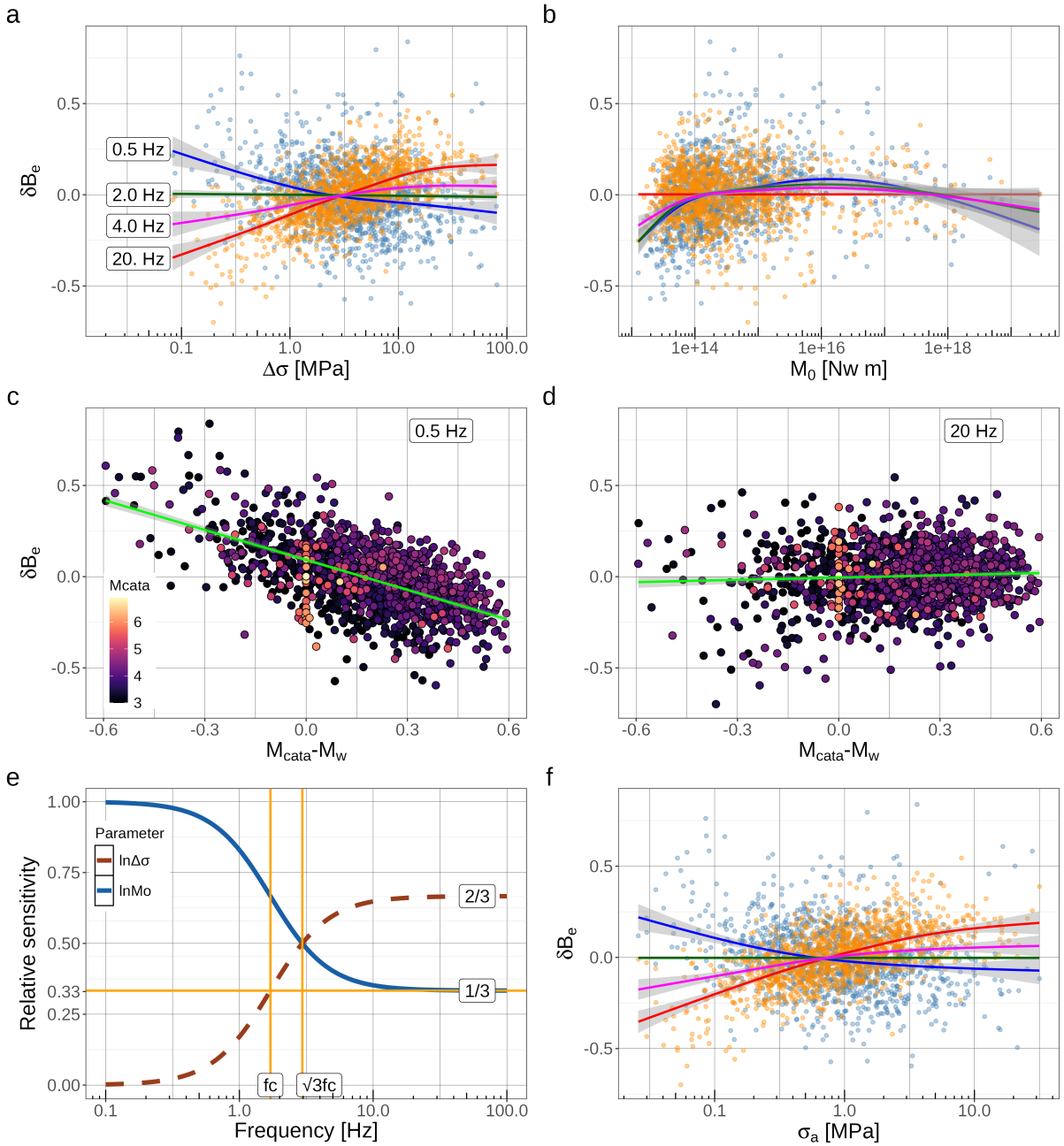


Figure 11 Panel a shows the between event residuals, δB_e, as computed by Brunelli et al. (2023), versus stress drop. The orange and blue circles represent the residuals at 20 Hz and 0.5 Hz, respectively. The colored lines show the results of Loess regressions performed for different frequencies, as indicated by the labels. Panel b shows the between event residuals versus seismic moment. The colors have the same meaning as in panel a. Panel c illustrates the between event residuals at 0.5 Hz versus the difference between the moment magnitude in the ITACAext flat file and the moment magnitude computed in this study. The green line is the result of a linear least squares regression. Panel d is the same as panel c but for 20 Hz. Panel e shows relative sensitivity (i.e., partial derivative normalized to the maximum) of the source spectrum with respect to the natural logarithm of stress drop (red) and to the natural logarithm of seismic moment (blue), as function of frequency. Panel f is the same as panel a but considering the apparent stress σ_a.

sensitivity of the source spectrum to $\Delta\sigma$ tends to zero at low frequencies. The negative correlation between δB_e at 0.5 Hz and the magnitude difference (panel c) could, at least partially, explain the negative trend of δB_e with $\Delta\sigma$. Since δB_e and the Mw values computed in this study are independent, whereas the δB_e at low frequencies are controlled by the catalog magnitude (M_{cata}), the positive δB_e values at 0.5 Hz in panel a for low $\Delta\sigma$ could reflect the underestimation of the catalog magnitudes with respect to Mw computed in this study ($\delta B_e > 0$ correspond to $M_{cata} - Mw < 0$, see panel c), in particular for small events (Kotha et al., 2022; Laurendeau and Kotha, 2024).

7 Discussion

Using the ITACAext dataset, we were able to consistently characterize source, propagation and site terms by analyzing the Fourier spectra of earthquakes of engineering interest that have been recorded in Italy since the 1970s.

Since the data set covers all Italy, we performed the spectral decomposition by considering a 2D attenuation model, defined over a regular grid. While a fully 3D reconstruction of the seismic attenuation would require a 3D velocity and attenuation tomography, the simplified 2D approach can be used to capture, at a first order, the impact of large scale lateral discontinuities. Before discussing the attenuation results, it is important to consider the limitations of this approach. Figure 1d shows that the rays crossing each grid cell are expected to propagate at different depths; in other words, the distributions characterizing the sampling at depth vary across the grid. Therefore, the 2D approach maps to the surface processes occurring at different depths for different cells. The resulting attenuation map should be interpreted in terms of large-scale contrasts to avoid over interpreting small-scale spatial patterns. Despite this limitation, the 2D grid approach provides a simple way to capture the primary impact of lateral variability in attenuation properties without requiring prior zonation and their associated epistemic uncertainty, thereby mitigating the transfer of attenuation effects to other terms in the decomposition.

The attenuation results (see Figure 4) show that the coefficients α are frequency-dependent, increasing in absolute value with frequency. In contrast, the geometrical spreading is almost frequency independent, with a slope between 1 and 1.2 for distances below 65 km, and a nearly flat trend between 65 and 130 km, where later arrivals, such as post-critical from the Moho, contribute to the wave field. The spatial distribution of α at high frequencies show spatial patterns that align with the expectations from the large-scale crustal structures and tectonics of Italy. For example, Mele et al. (1997) found that lower attenuation characterized propagation beneath the Alps and in the Adria foreland, which is consistent with a cold, thick, and mechanically strong lithosphere and slab fragments. Conversely, higher attenuation is observed beneath the Tyrrhenian back arc and parts of the Apennines, which matches expectations for a hot, thinned, possibly hydrated or partially molten mantle. More locally, high attenuation and high scattering anomalies, aligned with Quaternary extensional fault systems and fractured, fluid-rich zones along the Apennines, have been discussed by Talone et al. (2023). Adam Alddoum Adam et al. (2026) investigated the attenuation characteristics in Southern Apennines and the Calabria region. Here, distinct attenuation and scattering patterns are consistent with different lithospheric and slab geometries (e.g., Ionian subduction and slab retreat). The Southern Apennines exhibit high peak delays and high attenuation, which is indicative of strong scattering, a fluid-rich environment and heterogeneous crust. Figures 4 and 5 show that northern Sicily exhibits significantly higher attenuation than in the south. Northern Sicily is characterized by highly fractured crustal wedges. The presence of dense fault networks, intense crustal deformation, and local thermal anomalies (associated with the nearby volcanic arc and northern Sicilian thermal springs) promotes strong anelastic absorption and wave scattering, particularly at frequencies above 2 Hz. In contrast, the southern sector of the island, specifically the Hyblean Plateau, stands out as a prominent low-attenuation domain (Brunelli et al., 2023). This is due to cold, thick, and highly competent crust, characterized by low heat flow and an absence of major active internal fragmentation.

One of the aims of this study was to develop seismological models of the source, propagation and site effects, which could then be used to validate or interpret the random effects associated with non-ergodic ground models in Italy. In terms of attenuation, the α maps align with the zonation refined by Brunelli et al. (2023)) using the $\delta P2P$ residuals of their GMPM (see Figures 4 and 5). The distribution of α at high frequencies suggests that some zones in northern Italy could be merged or reshaped, though the main lateral contrasts at the national level align well with the zonation proposed by the $\delta P2P$ residuals. To provide an independent zonation, we used the gridded α values to define different data-driven zonation with an increasing level of complexity (see Figure 6). When the number of allowed zones is four, the identified zones are northern Italy (the central-eastern Alps and the Po Plain), two zones that separate the propagation in the Apennines towards the Tyrrhenian Sea and the Adriatic Sea, and the Hyblean plateau in southern Sicily (see Figure 6). These are the main domains for characterizing seismic attenuation at a national scale. Increasing the number of zones identifies smaller-scale domains which also align with expectations, such as the separation between the southern Apennines and the Calabrian arc or the geothermal areas in Tuscany. However, local studies are more suitable for pushing the zonation to this level of resolution (e.g. Bianco et al., 2005; Zolezzi et al., 2008; Akinci et al., 2020; Talone et al., 2023; De Gori et al., 2023; Gabrielli et al., 2023; Adam Alddoum Adam et al., 2026).

Using the grid approach to account for lateral variability in attenuation allowed us to obtain source parameters across the extensive and tectonically-complex area covered by ITACAext, thereby mitigating the source-attenuation trade-off. Unlike previous spectral decompositions, we removed the source-station trade-off by constraining the source parameters of three reference events using the results of a previous study (Bindi and Kotha, 2020). The suitability of the obtained source spectra is supported by the retrieved site amplifications. When we compared the results to the expected local effects at specific sites, we found good agreement, including the near-surface attenuation effects (Anderson and Hough, 1984).

In terms of source parameters and their scaling, the computed spectral stress drop shows an almost constant average value, with a slight tendency to increase for magnitudes greater than approximately 4.6 (i.e, $M_0 = 10^{16}$ Nm). This self-similar scaling contrasts with the results of recent studies which found an increase of stress drop with seismic moment for small-to-moderate events in various regions of Italy. Examples include studies for north eastern Italy (Cataldi et al., 2026), Emilia (De Gori et al., 2023), central Italy (Morasca et al., 2022), and Irpinia (Picozzi et al., 2021). It is difficult to compare the single components of spec-

tral decompositions performed by different studies and using different methodologies due to the inherent trade-offs between the terms (e.g. Abercrombie et al., 2025). One possible explanation for the different scaling obtained could be related to the fact that ITACAext differs from the data sets used in local/regional studies. ITACAext contains numerous mainshocks that occurred all over Italy, and include events with magnitudes mostly above 3.2. Regional data sets are often comprised of seismic sequences with many aftershocks, and magnitude distributions with barycentres shifted towards smaller magnitudes. Therefore, the composition of the data sets and the magnitude range sampled can both contribute to generating different scaling, since the observed positive trends of $\Delta\sigma$ with M_0 are mostly driven by earthquakes with magnitude smaller than 3.5.

A clear feature of the results in Figure 8 is the contrast in the population of events with $\Delta\sigma < 1$ MPa when the seismic moment crosses $\sim 10^{16}$ Nm. While we cannot rule out a methodological limitation related to the available bandwidth, which could affect the minimum resolvable corner frequency of large events with low stress drops, the broadening of the $\Delta\sigma$ distribution towards lower values for small to moderate events is a common feature observed in several studies (Abercrombie, 2021). Small and moderate-to-large earthquakes involve very different amounts of slip, and observations and dynamic models suggest that the dominant weakening and energy-dissipation processes may change with increasing slip (Viesca and Garagash, 2015; Gabriel et al., 2024). In this framework, ruptures occurring under very low driving stress may be more likely to arrest before reaching larger dimensions, so that very low stress-drop events would preferentially remain small. In conclusion, although we interpret the observed lower bound cautiously as it may result from spectral-resolution limits and is based on limited data, it is also consistent with physical constraints on rupture growth which could result in a magnitude-dependent minimum stress drop for large events.

The spatial distribution of the stress drop residuals identifies regions of stress drop higher than the values expected given the seismic moment (e.g., northern Italy and the Apulian foreland) and areas with lower than expected stress drop (e.g. central Adriatic sea, eastern Ionian). This is in agreement with the spatial distribution of δB_e at high frequencies in Brunelli et al. (2023) (their Figure 5) for regionalization of the source effects into GMPMs (Figure 11). The high stress drops in the Friuli region (zone EA in Figure 10), which is characterized by compressive tectonics and where the 1976, M_w 6.4 earthquake occurred, are consistent with the findings of several previous studies (e.g. Cocco and Rovelli, 1989; Castro et al., 1997), although the absolute values differ. The highest stress drops regarding the main shocks of the main normal-faulting sequences that occurred along the central and southern Apennines were obtained in the Irpinia area (zone IR in Figure 10), where the 1980, Mw 6.9 earthquake occurred. Both the Friuli and Irpinia areas exemplify how stress-drop patterns can be coherent over extremely variable scales ranging from a few kilometers to entire fault systems. Recent studies which analyzed data sets generated by local, dense seismic networks (see Picozzi et al. (2026); Cataldi et al. (2026) for Friuli and Zollo et al. (2014); Picozzi et al. (2021) for Irpinia) showed that stress drops in these areas were spatially heterogeneous. This reflects fault systems composed of segments with different mechanical characteristics, locking and creeping levels, and maturity. These studies, among many others, indicate that stress drop is not uniform across a fault system, earthquake sequence or crustal volume. Stress drop, apparent stress and seismic efficiency vary according to fault strength, effective stress, structural complexity, depth, lithology, stress orientation, rupture geometry and the local stage of the seismic cycle. A physical interpretation should therefore combine source parameters with focal mechanisms, fault geometry, depth, geodetic deformation and independent information on fluids or fault slip. However, this wide-spectrum analysis is well beyond the scope of our study.

8 Conclusions

We applied the spectral decomposition approach to the ITACAext dataset, which includes relevant engineering recordings from Italy since the 1970s. We implemented a 2D cell-grid approach to capture the lateral variability of attenuation without the need to introduce zonations a priori. We also introduced a constrained approach to overcome the trade-off between source and site terms based on the use of reference events. The main methodological conclusions are:

- The two grid inversion approaches tested (i.e. the mid-point and intersection approaches) produced similar results, as confirmed by the statistical parameters computed to quantify their differences. We opted for the intersection approach, as this is closer to the concept of 2D tomography and produces more resolved maps.
- The reference source approach was effective in overcoming the trade-off between source and site terms. The site amplification agrees well with previous studies, both in terms of the amplification pattern and near-surface high-frequency attenuation.

Regarding the attenuation results, the main conclusions are:

- the attenuation coefficients α are frequency-dependent, with clear spatial patterns emerging from approximately 2 Hz. The attenuation maps capture well the large-scale attenuation features expected for Italy considering its complex tectonics. The main attenuation domains are the central and eastern parts of northern Italy, the propagation from the Apennines towards the Tyrrhenian Sea and towards the Adriatic Sea, the Hyblean plateau. When more refined data-driven zonation are investigated, additional attenuation domains emerge (e.g., geothermal areas in Tuscany or the Calabrian back-arc).

- The attenuation patterns in the α map agree well with the attenuation zonation proposed by Brunelli et al. (2023) to describe the $\delta P2P$ spatial distribution of their non-ergodic GMPM.

- The geometrical spreading term, which is parametrized as a piecewise linear model with hinge distances of 65 and 130 km, is weakly dependent on frequency. The three branches have slopes that vary weakly around 1, 0 and 0.2, respectively. Considering the trade off between geometrical spreading and anelastic attenuation terms, these models should be used jointly.

Regarding the source results, the main conclusions are:

- the source parameters extracted from the non parametric spectra show, on average, a constant stress drop $\Delta\sigma$, with a median value of 3.64 MPa, and the 10th and 90th percentiles equal to 0.91 and 12.71 MPa, respectively. Above magnitude 4.6, the average $\Delta\sigma$ shows a slight tendency to increase but with values well within the overall scatter.

- the areas with the largest $\Delta\sigma$ are in northern Italy (average $\Delta\sigma$ = 11.48 MPa) and the Apulian foreland (average $\Delta\sigma$ = 9.33 MPa); the regions with the lowest average stress drop are the Ionian fault eastern lobe ($\Delta\sigma$ = 1.50 MPa) and the Adriatic Sea ($\Delta\sigma$ = 0.98 MPa). In term of scaled energy, the value of θ_k for magnitudes smaller than 4.6 ($M_0 = 10^{16}$ Nm) is -4.58; when computed for magnitudes greater than 5.6 ($M_0 = 10^{17.5}$ Nm), the average θ_k is -4.39.

- The spatial distribution of $\Delta\sigma$ agree well with the source zonation proposed by Brunelli et al. (2023) for the between events residuals δB_e. When compared for individual events, there is a strong correlation between δB_e and $\Delta\sigma$ at high frequencies, which then disappears at approximately 2 Hz. At low frequencies, however, there is an inverse correlation between $\Delta\sigma$ and the difference between the moment magnitude used to calibrate the GMPM and the moment magnitude computed from the seismic moment derived in this study.

In conclusion, the cell-grid spectral decomposition applied to the ITACAext dataset provides physically consistent models of source, propagation, and site amplification across Italy. The spatial coherence of these terms provides a valuable framework for interpreting the residuals of ground motion models in a physically meaningful way, supporting the development and validation of non-ergodic approaches. Moreover, these terms constitute natural building blocks for ground motion prediction models based on stochastic simulations.

Acknowledgements

We thank the two anonymous reviewers and the editor Pablo Heresi for their constructive comments and suggestions, which helped to improve the clarity and quality of the manuscript.

Data and code availability

The ITACAext flatfiles (v.1.0 and 2.0) are accessible at the permanent URL https://itaca.mi.ingv.it/ItacaNet_40/#/products/itacaext_flatfile. The accelerometric data used in ITACAext are all accessible through the ITalian ACcelerometric Archive (ITACA, https://itaca.mi.ingv.it/) and Engineering Strong Motion Database (ESM, https://esm-db.eu/) websites. Velocimeter records were extracted from the continuous streaming of stations available in European Integrated Data Archive (EIDA) at https://www.orfeus-eu.org/data/eida/. For this study, we did not download and analyze new waveforms, but started from the flatfiles that had already been compiled, i.e. from derived products. The networks registered with a DOI that originally contributed to the selected data set are: Institute of GeoSciences, Polytechnic University of Tirana (2002); ZAMG - Zentralanstalt für Meterologie und Geodynamik (1987); Epos-France (1995); RESIF (1995); Swiss Seismological Service (SED) At ETH Zurich (1983); Istituto Nazionale di Geofisica e Vulcanologia (INGV) (2005); University of Genoa (1967); Slovenian Environment Agency (1990); MedNet Project Partner Institutions (1990); Zhao et al. (2016); Presidency of Counsil of Ministers - Civil Protection Department (1972); Istituto Nazionale di Oceanografia e di Geofisica Sperimentale and University of Trieste (2002); Institut de physique du globe de Paris (IPGP) and École et Observatoire des sciences de la Terre de Strasbourg (EOST) (1982); University of Trieste (1993); National Observatory of Athens, Institute of Geodynamics, Athens (1975); Geological Survey-Provincia Autonoma di Trento (1981); Sector for Seismology, Institute of Hydrometeorology and Seismology of Montenegro (1982); Istituto Nazionale di Oceanografia e di Geofisica Sperimentale - OGS (2016); EMERSITO Working Group (2018); CERN (2016); Galluzzo et al. (2017); Art Lerner-Lam (2003); Presidenza del Consiglio dei Ministri - Dipartimento della protezione civile (2017); Alparone et al. (2021); Universita Della Calabria, Italy (1981); Vadim Levin (2003); Hetényi et al. (2017); Alparone et al. (2020); Massa et al. (2021); Piccinini et al. (2022); Pilz and Parolai (2009); D'Alema et al. (2022); Moretti et al. (2021); Helmstetter et al. (2020); Istituto Nazionale di Geofisica e Vulcanologia (INGV) et al. (2018); Istituto Nazionale di Geofisica e Vulcanologia (INGV) (2009); EMERSITO Working Group (2024); Marzorati et al. (2021). More information regarding contributing networks can be found in ITACA website at https://itaca.mi.ingv.it/ItacaNet_40/#/about/who/contributing_networks.

The decomposition results are available at 10.5281/zenodo.22734257. The repository includes a table of the source parameters and the spectral files for the source, attenuation and site amplifications. Analyses have been performed in R (R Core Team, 2024) using packages: ggplot2 (Wickham, 2016), dplyr (Wickham et al., 2022), sf (Pebesma, 2018), gstat (Gräler et al., 2016), sp (Pebesma and Bivand, 2005), osqp (Stellato et al., 2020), sparseM (Koenker and Ng, 2021), viridis (Garnier et al., 2021), cowplot (Wilke, 2020), rnaturalearth (Massicotte and South, 2023), patchwork (Ped-

ersen, 2025), DescTools (Signorell, 2025), rgeoda (Li and Anselin, 2026). The software project hosting the modules for spectral decomposition analysis is available at https://gitlab.rm.ingv.it/inversion/gitpy (Morasca et al., 2025).

Competing interests

The authors declare to have no competing interests.

References

Abercrombie, R. E. Resolution and uncertainties in estimates of earthquake stress drop and energy release. *Philosophical Transactions of the Royal Society A: Mathematical, Physical and Engineering Sciences*, 379(2196), 2021. doi: 10.1098/rsta.2020.0131.

Abercrombie, R. E., Baltay, A., Chu, S., Taira, T., Bindi, D., Boyd, O. S., Chen, X., Cochran, E. S., Devin, E., Dreger, D., Ellsworth, W., Fan, W., Harrington, R. M., Huang, Y., Kemna, K. B., Liu, M., Oth, A., Parker, G. A., Pennington, C., Picozzi, M., Ruhl, C. J., Shearer, P., Spallarossa, D., Trugman, D., Vandevert, I., Wu, Q., Yoon, C., Yu, E., Beroza, G. C., Eulenfeld, T., Knudson, T., Mayeda, K., Morasca, P., Neely, J. S., Roman-Nieves, J., Satriano, C., Supino, M., Walter, W. R., Archuleta, R., Atkinson, G. M., Calderoni, G., Ji, C., Yang, H., and Zhang, J. Overview of the SCEC/USGS Community Stress Drop Validation Study Using the 2019 Ridgecrest Earthquake Sequence. *Bulletin of the Seismological Society of America*, 115(3):734–759, 2025. doi: 10.1785/0120240158.

Adam Alddoum Adam, M., Totaro, C., Presti, D., Scolaro, S., and De Siena, L. Seismic attenuation and scattering tomography reveal lithospheric complexity and fluid signatures across the Southern Apennines–Northern Calabrian boundary (South Italy). *Geophysical Journal International*, 245(2):ggag111, 2026. doi: 10.1093/gji/ggag111.

Akinci, A., Pezzo, E. D., and Malagnini, L. Intrinsic and scattering seismic wave attenuation in the Central Apennines (Italy). *Physics of the Earth and Planetary Interiors*, 303:106498, 2020. doi: 10.1016/j.pepi.2020.106498.

Al Atik, L., Abrahamson, N., Bommer, J. J., Scherbaum, F., Cotton, F., and Kuehn, N. The Variability of Ground-Motion Prediction Models and Its Components. *Seismological Research Letters*, 81 (5):794–801, 09 2010. doi: 10.1785/gssrl.81.5.794.

Alparone, S., Cattaneo, M., Contrafatto, D., D'Alema, E., Franceschi, D., Larocca, G., Mandiello, A. G., Marzorati, S., Moretti, M., Piccinini, D., Rao, S., Salvaterra, L., and Speciale, S. Seismic Data acquired by the SISMIKO Emergency Group - Salemi-Italy 2020 - T15, 2020. doi: 10.13127/SD/LJFPEOSEK0.

Alparone, S., Cocina, O. M. G., Contrafatto, D., Larocca, G., Manni, M., Pruiti, L., Messina, A. A., Ursino, A., and D'Alema, E. Seismic Data acquired by the INGV temporary network for seismic monitoring of the island of Vulcano to increase volcanic activity (Sicily, Italy) - 2021, 2021. doi: 10.13127/SD/CFZ7FTSW-Y.

Anderson, J. G. and Hough, S. E. A model for the shape of the Fourier amplitude spectrum of acceleration at high frequencies. *Bulletin of the Seismological Society of America*, 74(5): 1969–1993, 10 1984. doi: 10.1785/BSSA0740051969.

Art Lerner-Lam. Calabria-Appennine-Tyrrhenian/Subduction-Collision-Accretion Network, 2003. doi: 10.7914/SN/YD_2003.

Babič, A., Abrahamson, N. A., Lavrentiadis, G., and Dolšek, M. Non-ergodic ground motion model using small-magnitude ground motion data for a site-specific PSHA in Slovenia. *Bulletin of Earthquake Engineering*, 24(6), 2026. doi: 10.1007/s10518-026-02395-y.

Baltay, A. S., Hanks, T. C., and Beroza, G. C. Stable Stress-Drop Measurements and their Variability: Implications for Ground-Motion Prediction. *Bulletin of the Seismological Society of America*, 103 (1):211–222, 02 2013. doi: 10.1785/0120120161.

Basili, R., Brizuela, B., Herrero, A., Iqbal, S., Lorito, S., Maesano, F. E., Murphy, S., Perfetti, P., Romano, F., Scala, A., Selva, J., Taroni, M., Tiberti, M. M., Thio, H. K., Tonini, R., Volpe, M., Glimsdal, S., Harbitz, C. B., Løvholt, F., Baptista, M. A., Carrilho, F., Matias, L. M., Omira, R., Babeyko, A., Hoechner, A., Gurbuz, M., Pekcan, O., Yalçıner, A., Canals, M., Lastras, G., Agalos, A., Papadopoulos, G., Triantafyllou, I., Benchekroun, S., Jaouadi, H. A., Attafi, K., Abdallah, S. B., Bouallegue, A., Hamdi, H., and Oueslati, F. NEAMTHM18 Documentation: the making of the TSUMAPS-NEAM Tsunami Hazard Model 2018, Sept. 2019. doi: 10.5281/zenodo.3406625.

Bianco, F., Pezzo, E. D., Malagnini, L., Luccio, F. D., and Akinci, A. Separation of depth-dependent intrinsic and scattering seismic attenuation in the northeastern sector of the Italian Peninsula. *Geophysical Journal International*, 161(1):130–142, 2005. doi: 10.1111/j.1365-246X.2005.02555.x.

Bindi, D. and Kotha, S. R. Spectral decomposition of the Engineering Strong Motion (ESM) flat file: regional attenuation, source scaling and Arias stress drop. *Bulletin of Earthquake Engineering*, 18:2581–2606, 04 2020. doi: 10.1007/s10518-020-00796-1.

Bindi, D., Parolai, S., Grosser, H., Milkereit, C., and Durukal, E. Empirical ground-motion prediction equations for northwestern Turkey using the aftershocks of the 1999 Kocaeli earthquake. *Geophysical Research Letters*, 34(8), 2007. doi: 10.1029/2007GL029222.

Bindi, D., Luzi, L., Parolai, S., Di Giacomo, D., and Monachesi, G. Site effects observed in alluvial basins: the case of Norcia (Central Italy). *Bull Earthquake Eng*, 9:1941–1959, 2011. doi: 10.1007/s10518-011-9273-3.

Bindi, D., Spallarossa, D., and Pacor, F. Between-event and between-station variability observed in the Fourier and response spectra domains: comparison with seismological models. *Geophysical Journal International*, 210(2):1092–1104, 2017. doi: 10.1093/gji/ggx217.

Bindi, D., Spallarossa, D., Picozzi, M., and Morasca, P. Reliability of Source Parameters for Small Events in Central Italy: Insights from Spectral Decomposition Analysis Applied to Both Synthetic and Real Data. *Bulletin of the Seismological Society of America*, 110(6):3139–3157, 2020. doi: 10.1785/0120200126.

Bindi, D., Spallarossa, D., Picozzi, M., Oth, A., Morasca, P., and Mayeda, K. The community stress-drop validation study—Part I: Source, propagation, and site decomposition of Fourier spectra. *Seismological Society of America*, 94(4):1980–1991, 2023. doi: 10.1785/0220230019.

Bindi, D., Mayeda, K., Spallarossa, D., Picozzi, M., Oth, A., Morasca, P., and Walter, W. R. Numerical Tests to Evaluate the Effect of Constraining the Spectral Shape of Reference Events on Source Parameter Scaling. *Bulletin of the Seismological Society of America*, 115(3):1062–1071, 2024. doi: 10.1785/0120240132.

Bindi, D., Picozzi, M., Oth, A., and Spallarossa, D. Impact of Seismic Attenuation Corrections on Source Parameter Estimation. *Seismica*, 4(2), 2025. doi: 10.26443/seismica.v4i2.1651.

Brune, J. N. Tectonic stress and the spectra of seismic shear waves from earthquakes. *Journal of Geophysical Research (1896-1977)*, 75(26):4997–5009, 1970. doi: 10.1029/JB075i026p04997.

Brune, J. N. Correction [to "Tectonic stress and the spectra, of seismic shear waves from earthquakes"]. *Journal of Geophysical Research (1896-1977)*, 76(20):5002–5002, 1971. doi: 10.1029/JB076i020p05002.

Brunelli, G., Lanzano, G., Luzi, L., and Sgobba, S. Data-driven

zonations for modelling the regional source and propagation effects into a Ground Motion Models in Italy. *Soil Dynamics and Earthquake Engineering*, 166:107775, 2023. doi: 10.1016/j.soildyn.2023.107775.

Castro, R., Pacor, F., and Petrungaro, C. Determination of S-wave energy release of earthquakes in the region of Friuli, Italy. *Geophysical Journal International*, 128(2):399–408, 1997. doi: 10.1111/j.1365-246X.1997.tb01563.x.

Castro, R. R., Anderson, J. G., and Singh, S. K. Site response, attenuation and source spectra of S waves along the Guerrero, Mexico, subduction zone. *Bulletin of the Seismological Society of America*, 80(6A):1481–1503, 1990. doi: 10.1785/BSSA08006A1481.

Cataldi, L., Picozzi, M., D'Amico, M., Morasca, P., Bindi, D., Poggi, V., Costa, G., Viganò, A., and Spallarossa, D. Stress drop and seismic efficiency distributions over the Adriatic indenter (European Southeastern Alps). *Journal of Geophysical Research - Solid Earth, accepted*, 2026.

CERN. CERN Seismic Network, 2016. doi: 10.12686/SED/NETWORKS/C4.

Cesca, S., Braun, T., Maccaferri, F., Passarelli, L., Rivalta, E., and Dahm, T. Source modelling of the M5–6 Emilia-Romagna, Italy, earthquakes (2012 May 20–29). *Geophysical Journal International*, 193(3):1658–1672, 2013. doi: 10.1093/gji/ggt069.

Chao, S.-H., Lin, C.-M., Kuo, C.-H., Huang, J.-Y., Wen, K.-L., and Chen, Y.-H. Implementing horizontal-to-vertical Fourier spectral ratios and spatial correlation in a ground-motion prediction equation to predict site effects. *Earthquake Spectra*, 37(2): 827–856, 2021. doi: 10.1177/8755293020952449.

Chen, K., Chen, X., Wang, Y., and Li, X. Source Scaling, Spatially Variable Path Attenuation, and Site-Effect Parameters via a Generalized Inversion Technique for Strong-Motion Data from Sichuan, China. *Bulletin of the Seismological Society of America*, 114(5): 2504–2523, 05 2024. doi: 10.1785/0120230268.

Chen, X. and Abercrombie, R. E. Improved approach for stress drop estimation and its application to an induced earthquake sequence in Oklahoma. *Geophysical Journal International*, 223 (1):233–253, 06 2020. doi: 10.1093/gji/ggaa316.

Cocco, M. and Rovelli, A. Evidence for the variation of stress drop between normal and thrust faulting earthquakes in Italy. *Journal of Geophysical Research: Solid Earth*, 94(B7):9399–9416, 1989. doi: 10.1029/JB094iB07p09399.

D'Alema, E., Alparone, S., Augliera, P., Biagini, D., Calamita, C., Castagnozzi, A., Cavaliere, A., Costanzo, A., Della Bina, E., Farroni, S., Galluzzo, D., Gasparini, A., Ladina, C., Lauciani, V., Mandiello, A. G., Margheriti, L., Marzorati, S., Moretti, M., Pantaleo, D., Pastori, M., Piccinini, D., Salimbeni, S., Scognamiglio, L., Zaccarelli, L., and Zuccarello, L. Seismic Data acquired by the SISMIKO Emergency Group - Northern Marche Coast - Italy 2022 - T17, 2022. doi: 10.13127/SD/TBLKBA-3U6.

Dawood, H. M. and Rodriguez-Marek, A. A Method for Including Path Effects in Ground-Motion Prediction Equations: An Example Using the Mw 9.0 Tohoku Earthquake Aftershocks. *Bulletin of the Seismological Society of America*, 103(2B):1360–1372, 2013. doi: 10.1785/0120120125.

De Gori, P., Pio Lucente, F., and Chiarabba, C. Source-Parameter Estimation after Attenuation Correction through the Use of Q Tomography. *Bulletin of the Seismological Society of America*, 113 (4):1739–1758, 2023. doi: 10.1785/0120220196.

Di Giulio, G., Rovelli, A., Cara, F., Azzara, R. M., Marra, F., Basili, R., and Caserta, A. Long-duration asynchronous ground motions in the Colfiorito plain, central Italy, observed on a two-dimensional dense array. *Journal of Geophysical Research: Solid Earth*, 108(B10), 2003. doi: 10.1029/2002JB002367.

Edwards, B., Rietbrock, A., Bommer, J. J., and Baptie, B. The Acquisition of Source, Path, and Site Effects from Microearthquake Recordings Using Q Tomography: Application to the United Kingdom. *Bulletin of the Seismological Society of America*, 98 (4):1915–1935, 08 2008. doi: 10.1785/0120070127.

Elzhov, T. V., Mullen, K. M., Spiess, A.-N., and Bolker, B. *minpack.lm: R Interface to the Levenberg-Marquardt Nonlinear Least-Squares Algorithm Found in MINPACK, Plus Support for Bounds*, 2023. https://CRAN.R-project.org/package=minpack.lm. R package version 1.2-4.

EMERSITO Working Group. Rete sismica del gruppo EMERSITO, sequenza sismica del 2016 in Italia Centrale, 2018. doi: 10.13127/SD/7TXEGDO5X8.

EMERSITO Working Group. Rete sismica temporanea 6N installata ad Ancona dal gruppo EMERSITO durante la sequenza sismica del 2022 - Costa Marchigiana-Pesarese, 2024. doi: 10.13127/SD/QCTGD6C-3A.

ENV 1998-1-1, E. . *Design provisions for earthquake resistance of structures. Seismic Actions and General Requirements of Structures, CEN/TC 250, Draft, May 2002*, 1998.

Epos-France. Epos-France Broad-band network (RLBP), 1995. doi: 10.15778/RESIF.FR.

Eshelby, J. D. The determination of the elastic field of an ellipsoidal inclusion, and related problems. *Proceedings of the Royal Society of London. Series A. Mathematical and Physical Sciences*, 241 (1226):376–396, 1957. doi: 10.1098/rspa.1957.0133.

Faccenna, C., Becker, T. W., Auer, L., Billi, A., Boschi, L., Brun, J. P., Capitanio, F. A., Funiciello, F., Horvàth, F., Jolivet, L., Piromallo, C., Royden, L., Rossetti, F., and Serpelloni, E. Mantle dynamics in the Mediterranean. *Reviews of Geophysics*, 52(3):283–332, 2014. doi: 10.1002/2013RG000444.

Gabriel, A.-A., Garagash, D. I., Palgunadi, K. H., and Mai, P. M. Fault size–dependent fracture energy explains multiscale seismicity and cascading earthquakes. *Science*, 385(6707):eadj9587, 2024. doi: 10.1126/science.adj9587.

Gabrielli, S., Akinci, A., De Siena, L., Del Pezzo, E., Buttinelli, M., Maesano, F. E., and Maffucci, R. Scattering Attenuation Images of the Control of Thrusts and Fluid Overpressure on the 2016-2017 Central Italy Seismic Sequence. *Geophysical Research Letters*, 50(8):e2023GL103132, 2023. doi: 10.1029/2023GL103132.

Galluzzo, D., Nardone, L., Gaudiosi, G., Martino, C., Scarpato, G., Carandente, A., Buonocunto, C., Govoni, A., Moretti, M., D'Alema, E., and SISMIKO Working Group. Seismic Data acquired by the SISMIKO Emergency Group - Ischia-Italy 2017 - T13, 2017. doi: 10.13127/SD/U0J8HSAEVF.

Garnier, Simon, Ross, Noam, Rudis, Robert, Camargo, Pedro, A., Sciaini, Marco, Scherer, and Cédric. *viridis - Colorblind-Friendly Color Maps for R*, 2021. doi: 10.5281/zenodo.4679424. R package version 0.6.2.

Geological Survey-Provincia Autonoma di Trento. Trentino Seismic Network, 1981. doi: 10.7914/SN/ST.

Gräler, B., Pebesma, E., and Heuvelink, G. Spatio-Temporal Interpolation using gstat. *The R Journal*, 8:204–218, 2016.

Grendas, I., Theodoulidis, N., Hollender, F., and Hatzidimitriou, P. Spectral decomposition of S-waves in investigating regional dependent attenuation and improving site amplification factors: A case study in western Greece. *Bulletin of Earthquake Engineering*, 20(12):1573–1456, 2022. doi: 10.1007/s10518-022-01459-z.

Helmstetter, A., Gueguen, P., and RESIF. Seismic network 8C :monitoring swarms in the Mont-Blanc and Vallorcine area (RESIF - SISMOB), 2020. doi: 10.15778/RESIF.8C2019.

Hetényi, G., Plomerová, J., Solarino, S., Scarponi, M., Vecsey, L., Munzarová, H., Babuška, V., Jedlička, P., Kotek, J., and Colavitti, L. Ivreaarray - An Alparray Complementary Experiment, 2017.

doi: 10.5281/ZENODO.1038209.

Ide, S. and Beroza, G. C. Does apparent stress vary with earthquake size? *Geophysical Research Letters*, 28(17):3349–3352, 2001. doi: 10.1029/2001GL013106.

Institut de physique du globe de Paris (IPGP) and École et Observatoire des sciences de la Terre de Strasbourg (EOST). GEOSCOPE, French Global Network of broad band seismic stations, 1982. doi: 10.18715/GEOSCOPE.G.

Institute of GeoSciences, Polytechnic University of Tirana. Albanian Seismological Network, 2002. doi: 10.7914/SN/AC.

Istituto Nazionale di Geofisica e Vulcanologia . Database of Individual Seismogenic Sources (DISS), Version 3.3.1: A compilation of potential sources for earthquakes larger than M 5.5 in Italy and surrounding areas, 2025. doi: 10.13127/diss3.3.1.

Istituto Nazionale di Geofisica e Vulcanologia (INGV). Rete Sismica Nazionale (RSN), 2005. doi: 10.13127/SD/X0FXNH7QFY.

Istituto Nazionale di Geofisica e Vulcanologia (INGV). Emersito Seismic Network for Site Effect Studies in L'Aquila town (Central Italy), 2009. doi: 10.7914/SN/4A_2009.

Istituto Nazionale di Geofisica e Vulcanologia (INGV), Istituto di Geologia Ambientale e Geoingegneria (CNR-IGAG), Istituto per la Dinamica dei Processi Ambientali (CNR-IDPA), Istituto di Metodologie per l'Analisi Ambientale (CNR-IMAA), and Agenzia Nazionale per le nuove tecnologie, l'energia e lo sviluppo economico sostenibile (ENEA). Rete del Centro di Microzonazione Sismica (CentroMZ), sequenza sismica del 2016 in Italia Centrale, 2018. doi: 10.13127/SD/KU7XM12YY9.

Istituto Nazionale di Oceanografia e di Geofisica Sperimentale - OGS. North-East Italy Seismic Network, 2016. doi: 10.7914/SN/OX.

Istituto Nazionale di Oceanografia e di Geofisica Sperimentale and University of Trieste. North-East Italy Broadband Network, 2002. doi: 10.7914/SN/NI.

Izutani, Y. and Kanamori, H. Scale-dependence of seismic energy-to-moment ratio for strike-slip earthquakes in Japan. *Geophysical Research Letters*, 28(20):4007–4010, 2001. doi: 10.1029/2001GL013402.

Kanamori, H. The energy release in great earthquakes. *Journal of Geophysical Research*, 82(20):2981–2987, 1977. doi: 10.1029/JB082I020P02981.

Koenker, R. and Ng, P. SparseM: Sparse Linear Algebra. *R package version 1.81*, 2021. https://CRAN.R-project.org/package=SparseM.

Konno, K. and Ohmachi, T. Ground-motion characteristics estimated from spectral ratio between horizontal and vertical components of microtremor. *Bulletin of the Seismological Society of America*, 88(1):228–241, 1998. doi: 10.1785/BSSA0880010228.

Kotha, S. R., Weatherill, G., Bindi, D., and Cotton, F. Near-source magnitude scaling of spectral accelerations: analysis and update of Kotha et al. (2020) model. *Bulletin of Earthquake Engineering*, 20:1343–1370, 2022. doi: 10.1007/s10518-021-01308-5.

Kwiatek, G. and Ben-Zion, Y. Theoretical limits on detection and analysis of small earthquakes. *Journal of Geophysical Research: Solid Earth*, 121(8):5898–5916, 2016. doi: 10.1002/2016JB012908.

Lanzano, G., Vitrano, L., Bindi, D., Felicetta, C., Sgobba, S., Luzi, L., and Pacor, F. ITACAext 2.0: A High-Quality Parametric Table of Strong-to-Weak Motion Recordings for Seismological and Engineering Research in Italy. *Seismological Research Letters*, 96(5): 3295–3316, 2025. https://doi.org/10.1785/0220240309.

Laurendeau, A. and Kotha, S. Impact of Mw definition approach on Fourier ground-motion variability of shallow crustal earthquakes in Europe. *J.Seismol*, pages 127–145, 2024. doi: 10.1007/s10950-024-10254-z.

Lavrentiadis, G., Abrahamson, N., and Kuehn, N. A non-ergodic effective amplitude ground-motion model for California. *Bulletin of Earthquake Engineering*, pages 5233–5264, 2023. doi: 10.1007/s10518-021-01206-w.

Li, X. and Anselin, L. *rgeoda: R Library for Spatial Data Analysis*, 2026. doi: 10.32614/CRAN.package.rgeoda. R package version 0.1.1.

Liu, C., Macedo, J., Abrahamson, N., Lacour, M., Gulerce, Z., Kottke, A., and Arda Ozacar, A. Modeling Path Effects Due to 3D Velocity Structure for Nonergodic Ground-Motion Models: A Case Study Using Turkish Ground-Motion Data. *Bulletin of the Seismological Society of America*, 115(2):602–618, 2025. doi: 10.1785/0120240055.

Luzi, L., D'Amico, M., Massa, M., and Puglia, R. Site effects observed in the Norcia intermountain basin (Central Italy) exploiting a 20-year monitoring. *Bull Earthquake Eng*, 17:97–118, 2019. doi: 10.1007/s10518-018-0444-3.

Marzorati, S., Ladina, C., Pantaleo, D., Calamita, C., Sofia, S., Boccanera, F., and Speranza, G. Seismic Data acquired by Snowbilla network - Sibillini Mountains - Italy, 2021. doi: 10.13127/SD/FCJDR8KEY3.

Massa, M., Rizzo, A. L., Lorenzetti, A., Lovati, S., D'Alema, E., Puglia, R., Carannante, S., and Luzi, L. Rete di monitoraggio multiparametrico del Garda (Nord Italia) - PDnet, 2021. doi: 10.13127/SD/YHCFOMCBO_.

Massicotte, P. and South, A. *rnaturalearth: World Map Data from Natural Earth*, 2023. https://CRAN.R-project.org/package=rnaturalearth. R package version 1.0.1.

MedNet Project Partner Institutions. Mediterranean Very Broadband Seismographic Network (MedNet), 1990. doi: 10.13127/SD/FBBBTDTD6Q.

Mele, G., Rovelli, A., Seber, D., and Barazangi, M. Shear wave attenuation in the lithosphere beneath Italy and surrounding regions: Tectonic implications. *Journal of Geophysical Research: Solid Earth*, 102(B6):11863–11875, 1997. doi: 10.1029/97JB00262.

Morasca, P., Bindi, D., Mayeda, K., Roman-Nieves, J., Barno, J., Walter, W. R., and Spallarossa, D. Source scaling comparison and validation in Central Italy: data intensive direct S waves versus the sparse data coda envelope methodology. *Geophysical Journal International*, 231:1573–1590, 2022. doi: 10.1093/gji/ggac268.

Morasca, P., D'Amico, M., Spallarossa, D., Bindi, D., Picozzi, M., Oth, A., and Pacor, F. GITpy: A Python Implementation of the Generalized Inversion Technique. *Seismological Research Letters*, 96 (6):3866–3879, 2025. doi: 10.1785/0220250042.

Moretti, M., Margheriti, L., Alparone, S., Costanzo, A., La Rocca, M., Murphy, S., Gutscher, M.-A., and Focus Working Group. Seismic Data acquired by FocusX temporary land-network (FXland), Southern Italy, 2021. https://eida.ingv.it/en/network/1J_2021.

National Observatory of Athens, Institute of Geodynamics, Athens. Hellenic Unified Seismological Network, 1975. doi: 10.7914/SN/HL.

Newman, A. V. and Okal, E. A. Teleseismic estimates of radiated seismic energy: The E/M_0 discriminant for tsunami earthquakes. *Journal of Geophysical Research: Solid Earth*, 103(B11): 26885–26898, 1998. doi: 10.1029/98JB02236.

Nie, S. and Wang, Y. Revealing Spatial Variations of Earthquake Stress Drop and Peak Ground Acceleration Using a Non-Ergodic Modeling Framework. *Geophysical Research Letters*, 52(5): e2024GL112043, 2025. doi: 10.1029/2024GL112043.

Openshaw, S. Optimal Zoning Systems for Spatial Interaction Models. *Environment and Planning A: Economy and Space*, 9(2):

169–184, 1977. doi: 10.1068/a090169.

Oth, A., Miyake, H., and Bindi, D. On the relation of earthquake stress drop and ground motion variability. *Journal of Geophysical Research: Solid Earth*, 122(7):5474–5492, 2017. doi: 10.1002/2017JB014026.

Pebesma, E. Simple Features for R: Standardized Support for Spatial Vector Data. *The R Journal*, 10(1):439–446, 2018. doi: 10.32614/RJ-2018-009.

Pebesma, E. J. and Bivand, R. Classes and methods for spatial data in R. *R News*, 5(2):9–13, 2005. https://CRAN.R-project.org/doc/Rnews/.

Pedersen, T. L. *patchwork: The Composer of Plots*, 2025. doi: 10.32614/CRAN.package.patchwork. R package version 1.3.2.

Piccinini, D., Biagini, D., D'Ambrosio, M., D'Alema, E., Zuccarello, L., Saccorotti, G., Pastori, M., Carluccio, I., Fares, M., Della Bina, E., Quintiliani, M., Lauciani, V., Criscuoli, F., De Gori, P., Mandiello, A. G., Scognamiglio, L., Moretti, M., Marzorati, S., and SISMIKO Working Group. Seismic Data acquired by the SISMIKO Emergency Group - Chianti Fiorentino - Italy 2022 - T16, 2022. doi: 10.13127/SD/JHGGG3BNLQ.

Picozzi, M., Bindi, D., Festa, G., Cotton, F., Scala, A., and D'Agostino, N. Spatiotemporal Evolution of Microseismicity Seismic Source Properties at the Irpinia Near-Fault Observatory, Southern Italy. *Bulletin of the Seismological Society of America*, 112(1):226–242, 2021. doi: 10.1785/0120210064.

Picozzi, M., Spallarossa, D., and Bindi, D. Spatiotemporal variations in b-value suggest an evolving mechanical state of the crust in the southeastern Alps. *Sci Rep*, 16:23047, 2026. doi: 10.1038/s41598-026-51916-x.

Pilz, M. and Parolai, S. Norcia basin (Italy) temporary seismic network, 2009. doi: 10.14470/8U7554472182.

Pondrelli, S., Salimbeni, S., Perfetti, P., and Danecek, P. Quick Regional Centroid Moment Tensor Solutions for the Emilia 2012 (northern Italy) Seismic Sequence. *Ann. Geohys*, 55(4), 2012. doi: 10.4401/ag-6146.

Presidency of Counsil of Ministers - Civil Protection Department . Italian Strong Motion Network, 1972. doi: 10.7914/SN/IT.

Presidenza del Consiglio dei Ministri - Dipartimento della protezione civile. Reti accelerometriche centri storici italiani, 2017. doi: 10.7914/SN/RR.

R Core Team. *R: A Language and Environment for Statistical Computing*. R Foundation for Statistical Computing, Vienna, Austria, 2024. https://www.R-project.org/.

RESIF. RESIF-RAP French Accelerometric Network, 1995. doi: 10.15778/RESIF.RA.

Savage, J. C. and Wood, M. D. The relation between apparent stress and stress drop. *Bulletin of the Seismological Society of America*, 61(5):1381–1388, 1971. doi: 10.1785/BSSA0610051381.

Sector for Seismology, Institute of Hydrometeorology and Seismology of Montenegro. Montenegrin Seismic Network, 1982. doi: 10.7914/SN/ME.

Sgobba, S., Lanzano, G., Pacor, F., Puglia, R., D'Amico, M., Felicetta, C., and Luzi, L. Spatial Correlation Model of Systematic Site and Path Effects for Ground-Motion Fields in Northern Italy. *Bulletin of the Seismological Society of America*, 109(4):1419–1434, 2019. doi: 10.1785/0120180209.

Sgobba, S., Felicetta, C., Bortolotti, T., Menafoglio, A., Lanzano, G., and Pacor, F. A geostatistical modelling of empirical amplification functions and related site proxies for shaking scenarios in central Italy. *Soil Dynamics and Earthquake Engineering*, 179: 108496, 2024. doi: 10.1016/j.soildyn.2024.108496.

Shearer, P. M., Prieto, G. A., and Hauksson, E. Comprehensive analysis of earthquake source spectra in southern California. *Journal of Geophysical Research: Solid Earth*, 111(B6), 2006. doi: 10.1029/2005JB003979.

Signorell, A. *DescTools: Tools for Descriptive Statistics*, 2025. doi: 10.32614/CRAN.package.DescTools. R package version 0.99.60.

Slovenian Environment Agency. Seismic Network of the Republic of Slovenia, 1990. doi: 10.7914/SN/SL.

Stellato, B., Banjac, G., Goulart, P., Bemporad, A., and Boyd, S. OSQP: an operator splitting solver for quadratic programs. *Mathematical Programming Computation*, 12(4):637–672, 2020. doi: 10.1007/s12532-020-00179-2.

Stewart, J. P., Afshari, K., and Goulet, C. A. Non-Ergodic Site Response in Seismic Hazard Analysis. *Earthquake Spectra*, 33(4): 1385–1414, 2017. doi: 10.1193/081716eqs135m.

Swiss Seismological Service (SED) At ETH Zurich. National Seismic Networks of Switzerland, 1983. doi: 10.12686/SED/NETWORKS/CH.

Talone, D., De Siena, L., Lavecchia, G., and de Nardis, R. The Attenuation and Scattering Signature of Fluid Reservoirs and Tectonic Interactions in the Central-Southern Apennines (Italy). *Geophysical Research Letters*, 50(22):e2023GL106074, 2023. doi: 10.1029/2023GL106074.

Taylor, K. E. Summarizing multiple aspects of model performance in a single diagram. *Journal of Geophysical Research: Atmospheres*, 106(D7):7183–7192, 2001. doi: 10.1029/2000JD900719.

Trugman, D. T. and Shearer, P. M. Strong Correlation between Stress Drop and Peak Ground Acceleration for Recent M 1–4 Earthquakes in the San Francisco Bay Area. *Bulletin of the Seismological Society of America*, 108(2):929–945, 2018. doi: 10.1785/0120170245.

Universita Della Calabria, Italy. Rete Sismica Unical, 1981. doi: 10.7914/SN/IY.

University of Genoa. Regional Seismic Network of North Western Italy, 1967. doi: 10.7914/SN/GU.

University of Trieste. Friuli Venezia Giulia Accelerometric Network, 1993. doi: 10.7914/SN/RF.

Vadim Levin. Retreating-Trench, Extension, and Accretion LTectonics: A Multidisciplinary Study of the Northern Apennines, 2003. doi: 10.7914/SN/YI_2003.

Viesca, R. C. and Garagash, D. I. Ubiquitous weakening of faults due to thermal pressurization. *Nature Geosci*, pages 875–879, 2015. doi: 10.1038/ngeo2554.

Visini, F., Meletti, C., Rovida, A., D'Amico, V., Pace, B., and Pondrelli, S. An updated area-source seismogenic model (MA4) for seismic hazard of Italy. *Natural Hazards and Earth System Sciences*, 22 (8):2807–2827, 2022. doi: 10.5194/nhess-22-2807-2022.

Wickham, H. *ggplot2: Elegant Graphics for Data Analysis*. Springer-Verlag New York, 2016. https://ggplot2.tidyverse.org.

Wickham, H., François, R., Henry, L., and Müller, K. *dplyr: A Grammar of Data Manipulation*, 2022. https://CRAN.R-project.org/package=dplyr. R package version 1.0.8.

Wilke, C. O. *cowplot: Streamlined Plot Theme and Plot Annotations for 'ggplot2'*, 2020. https://CRAN.R-project.org/package=cowplot. R package version 1.1.1.

Wyss, M. Stress estimates for South American shallow and deep earthquakes. *Journal of Geophysical Research (1896-1977)*, 75 (8):1529–1544, 1970. doi: 10.1029/JB075i008p01529.

Yen, M.-H., Bindi, D., Oth, A., Edwards, B., Zaccarelli, R., and Cotton, F. Source parameters and scaling relationships of stress drop for shallow crustal seismic events in Western Europe. *Journal of Seismology*, 28:63–79, 2024. doi: 10.1007/s10950-023-10188-y.

ZAMG - Zentralanstalt für Meterologie und Geodynamik. Austrian

Seismic Network, 1987. doi: 10.7914/SN/OE.

Zhao, L., Paul, A., Solarino, S., and RESIF. Seismic network YP: CIFALPS temporary experiment (China-Italy-France Alps seismic transect), 2016. doi: 10.15778/RESIF.YP2012.

Zolezzi, F., Morasca, P., Mayeda, K., Phillips, W. S., and Eva, C. Attenuation tomography of the Southern Apennines (Italy). *Journal of Seismology*, 12:355–365, 2008. doi: 10.1007/s10950-007-9079-6.

Zollo, A., Orefice, A., and Convertito, V. Source parameter scaling and radiation efficiency of microearthquakes along the Irpinia fault zone in southern Apennines, Italy. *Journal of Geophysical Research: Solid Earth*, 119(4):3256–3275, 2014. doi: 10.1002/2013JB010116.

The article *Cell-Based Spectral Decomposition of Strong Ground Motion Data for Seismic Source and Attenuation Characterization in Italy* © 2026 by Dino Bindi is licensed under CC BY 4.0.